DEFORMATION AND FRACTURE MECHANISMS IN IRRADIATED FCC AND BCC METALS–S.J. Zinkle (Oak Ridge National Laboratory) and G.E. Lucas (University of California-Santa Barbara)

OBJECTIVE

The objective of this report is to assess deformation mechanisms in several irradiated alloy systems that are of interest for fusion energy applications.

SUMMARY

The effects of irradiation on the mechanical behavior of face-centered cubic (FCC) and body centered cubic (BCC) metals are briefly reviewed, including dislocation channeling, cleavage fracture, and irradiation creep at low irradiation temperatures and helium grain boundary embrittlement at high temperatures. Particular emphasis is placed on the microstructural mechanisms responsible for the changes in mechanical behavior. Four different material systems are examined as typical examples of behavior in FCC (dispersion strengthened and precipitation strengthened copper, Type 316 austenitic stainless steel) and BCC (V-Cr-Ti alloys, 8-9 Cr ferritic/martensitic steel) metals. Similarities and differences in the mechanical behavior of irradiated FCC and BCC metals are highlighted. The stress and temperature regimes where various deformation mechanisms predominate before and after irradiation are displayed in terms of Ashby deformation maps. Tensile tests can often provide a misleading indication of the fracture toughness behavior due to the lack of stress concentrators in un-notched specimens.

PROGRESS AND STATUS

1. Introduction

Irradiation can produce dramatic changes in the mechanical properties of metals [1-7]. For example, early studies on irradiated metals [3,4,8,9] clearly demonstrated that irradiation at low temperatures (<0.3 T_M, where T_M is the melting temperature) produced pronounced hardening. The hardening is typically accompanied by a severe decrease in uniform plastic elongation as measured in a uniaxial tensile test [1-3]. Embrittlement as measured by decreases in fracture toughness and increases in the ductile to brittle transition temperature (DBTT) of BCC alloys are commonly observed consequences of low temperature irradiation hardening [10-13]. Irradiation creep [14,15] and high temperature He embrittlement of grain boundaries [16,17] are examples of additional mechanical property degradation processes that occur in irradiated metals at progressively higher temperatures.

The decrease in tensile ductility associated with low temperature neutron irradiation was the topic of numerous studies performed in the 1960s, and the phenomenon was commonly referred to as "low temperature radiation embrittlement". However, these early studies did not attempt to measure the fracture toughness of irradiated specimens. As will be discussed in section 4 of this paper, tensile "embrittlement" does not universally correlate with fracture toughness embrittlement and there are numerous examples now available where high dynamic and/or quasi-static toughness is maintained in irradiated metals that exhibit low uniform elongations. A more appropriate term for the low uniform elongation typically observed following low-temperature irradiation is “loss of strain hardening capacity” (which may or may not be associated with a reduction in fracture toughness).

The present paper will focus on the mechanical properties of four FCC and BCC alloy systems before and after irradiation. Copper alloys (GlidCop Al25 oxide dispersion strengthened copper, CuCrZr and CuNiBe) and Type 316 austenitic stainless steel were chosen as representative FCC metals. V-4%Cr-4%Ti and 8-9%Cr ferritic/martensitic steels have been chosen to demonstrate behavior observed in BCC metals. Ashby-type maps [18] have been constructed in order to assist in the identification of the various deformation processes that occur at different stresses and temperatures before and after irradiation.

2. Fundamentals of radiation hardening at low temperatures

Irrespective of the alloy type or crystal structure, a general feature associated with irradiation at low temperature (below ~0.3 T_M) is increased matrix hardness due to the presence of radiation-induced defects which act as obstacles to dislocation motion. Figure 1 shows the yield strength of copper as a function of damage level for irradiation near room temperature [19-26]. The yield strength increases with increasing dose up to ~0.1 displacements per atom (dpa), and then reaches an apparent "saturation hardening" regime where the yield strength remains nearly constant (~300 MPa) as the dose is increased. A similar low-dose rapid hardening regime followed by a slowly evolving hardening behavior at higher doses has been observed in several other FCC and BCC metals irradiated at low temperatures, although materials such as austenitic and ferritic-martensitic stainless steel maintain a slight positive slope in the "saturation hardening" regime [27-30].

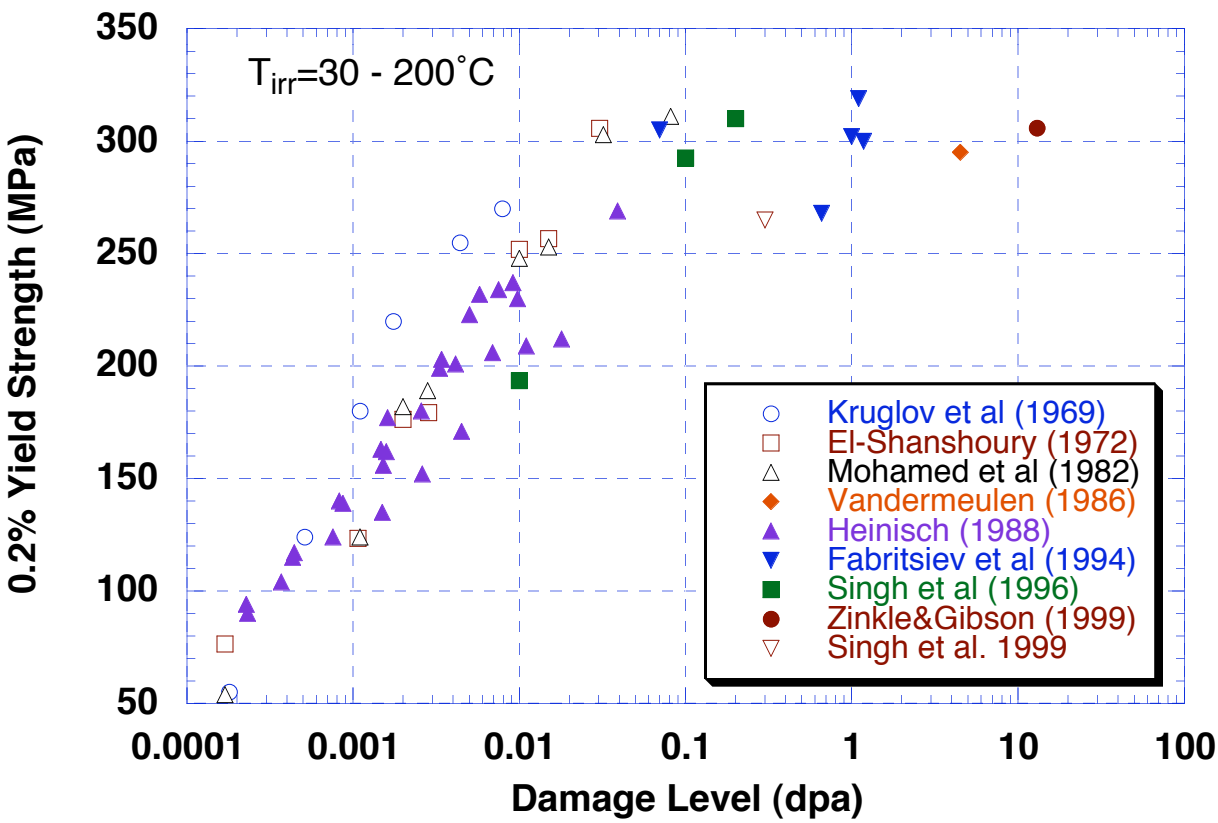

Fig. 1. Dose dependence of radiation hardening in pure copper irradiated with neutrons at 30-200˚C [19-26].

The increase in matrix hardness at low irradiation temperatures is due to the presence of small radiation-induced clusters of vacancies and self-interstitial atoms. From simple geometric considerations of a dislocation traversing a slip plane which intersects randomly distributed obstacles of diameter d and atomic density N, and using the approximation for dislocation line tension $T \sim 0.5\mu b^2$, the increase in the critical resolved shear stress ($\Delta\tau$) in a pure metal is given by the well-known dispersed barrier hardening equation [5,31,32]

$$\Delta\tau = \alpha\mu b(Nd)^{1/2} \qquad (1)$$

where μ is the shear modulus, b is the magnitude of the Burgers vector of the glide dislocation ($a_0/\sqrt{2}$ for FCC, $\sqrt{3}\,a_0/2$ for BCC, where a_0 is the lattice parameter), and α is average barrier strength of the radiation-

induced defect clusters. Early experimental estimates of the barrier strength of defect clusters produced during low-temperature neuron irradiation were typically α~0.5. More recent experimental estimates (obtained on electron microscopes with improved resolution in order to detect small defect clusters) range from α~0.10-0.25 for copper [33,34], austenitic stainless steel [32,35], and V-4Cr-4Ti [36] irradiated at low temperatures. Since the mean defect cluster size changes very slowly at these low irradiation temperatures, the increase in strength (eqn. 1) is mainly due to an increase in the defect cluster density at low doses. Transmission electron microscopy studies of metals irradiated at low temperature [36,37] have observed that the defect cluster density typically reaches an apparent saturation value of ~$1x10^{24}$ to $1x10^{24}m^3$ at doses above ~0.1 dpa. Pure Fe is known to be an exception to this general trend; saturation in the visible black spot defect cluster density has not been observed in Fe following irradiation near room temperature to doses in excess of 0.3 dpa [38].

The appropriate dislocation barrier superposition rules need to be considered when analyzing radiation hardening in alloys. Depending on the relative barrier strength of the hardening agents in the alloy (solid solution hardening, precipitation hardening, etc.), the radiation hardening component may be given by a square root summation of the squares of the preirradiation and irradiation hardening components (or more complex superposition equations), rather than a simple linear superposition [4,39,40].

For polycrystalline specimens, the uniaxial tensile stress is related to the critical resolved shear stress by the Taylor factor (M):

$$\sigma = M \tau \qquad (2)$$

where M equals 3.06 for equiaxed FCC and BCC metals [41]. It should be noted that several studies have found evidence that the rate of radiation hardening increases with decreasing grain size [3,9,42,43]. On the other hand, conflicting results on the effect of grain size have been obtained in BCC metals such as Fe [4,44,45]. Further work is needed to determine the quantitative significance (and possible physical mechanisms) of this effect [32]. If a radiation modified grain size effect exists, the value of α determined from studies on polycrystalline specimens is an upper limit to the value appropriate for large-grained or single crystal specimens.

A characteristic feature that accompanies the pronounced hardening in metals irradiated at temperatures below electrical resistivity recovery stage V (~0.35 T_M) is loss of work hardening capacity. Early studies of radiation hardening produced competing models for the hardening mechanism, based on “dislocation source locking” and “lattice friction” concepts. Several researchers have proposed that both mechanisms operate, with source hardening responsible for the upper yield point and lattice hardening responsible for the lower yield stress observed in metals irradiated at low temperatures [38,46-48]. The loss of work hardening capacity produces sharp decreases in uniform elongation. Both effects have been shown to be generally due to dislocation channeling [2,36,38,49-55]. Dislocation channeling occurs because the radiation-induced defect clusters present at these low temperatures can be readily cut by gliding dislocations (α~0.1-0.25, as opposed to 0.8 for impenetrable Orowan obstacles). This produces a defect-free path for subsequent dislocations emitted from the operating source [2,38,50-54,56-66]. Dislocation channeling begins to occur above a critical dose/hardening level (corresponding to N>~$1x10^{24/}m^3$ for copper tested at room temperature [32]). At low doses, the presence of dislocation channeling may also depend on the amount of deformation [53] (channeling is present at low levels of deformation, whereas the deformation mode reverts to cell structure at high levels of deformation/stress). Twinning has also been observed to cause a pronounced loss in strain hardening capacity in austenitic stainless steel irradiated at 290˚C and tested near room temperature [66-68].

3. Brief overview of deformation behavior of irradiated metals

Several aspects of the deformation behavior of irradiated BCC and FCC metals are qualitatively similar. In particular, the physical phenomenon of dislocation channeling has been observed in numerous BCC, FCC, and hexagonal close-packed metals following neutron irradiation at temperatures below ~0.3 T_M [2,38,69,70]. The irradiation creep compliance of BCC and FCC steels at moderate temperatures are within a factor of two of each other [14,71,72]. Finally, high temperature He embrittlement of grain boundaries has been observed to occur in numerous BCC and FCC metals and alloys at irradiation temperatures above 0.5 T_M [16,17,73,74], although the threshold helium concentration for pronounced

high temperature embrittlement has been observed to be significantly higher in ferritic/martensitic steels compared to austenitic stainless steels. For high levels of radiation hardening, cleavage fracture can be induced in BCC alloys due to the well-known Ludwig-Davidenkov relationship (due to the localized stress exceeding the cleavage stress) [10].

Radiation hardening is typically most pronounced in BCC and FCC metals following irradiation at low temperatures [13,29,75,76] (neutron irradiated stainless steel being a notable exception [28,77]). Figure 2 summarizes the yield strength vs. temperature for unirradiated and neutron irradiated GlidCop Al25 oxide dispersion strengthened copper [26,78,79]. The yield strength of GlidCop following neutron irradiation is significantly higher than the unirradiated yield strength for irradiation temperatures up to ~300˚C. At irradiation and test temperatures above ~300˚C, the yield strength of irradiated GlidCop is comparable to that of unirradiated specimens. The temperature-dependent increase in strength of the irradiated pure copper and copper alloy specimens can be directly correlated with the temperature-dependent defect cluster density produced by irradiation [32].

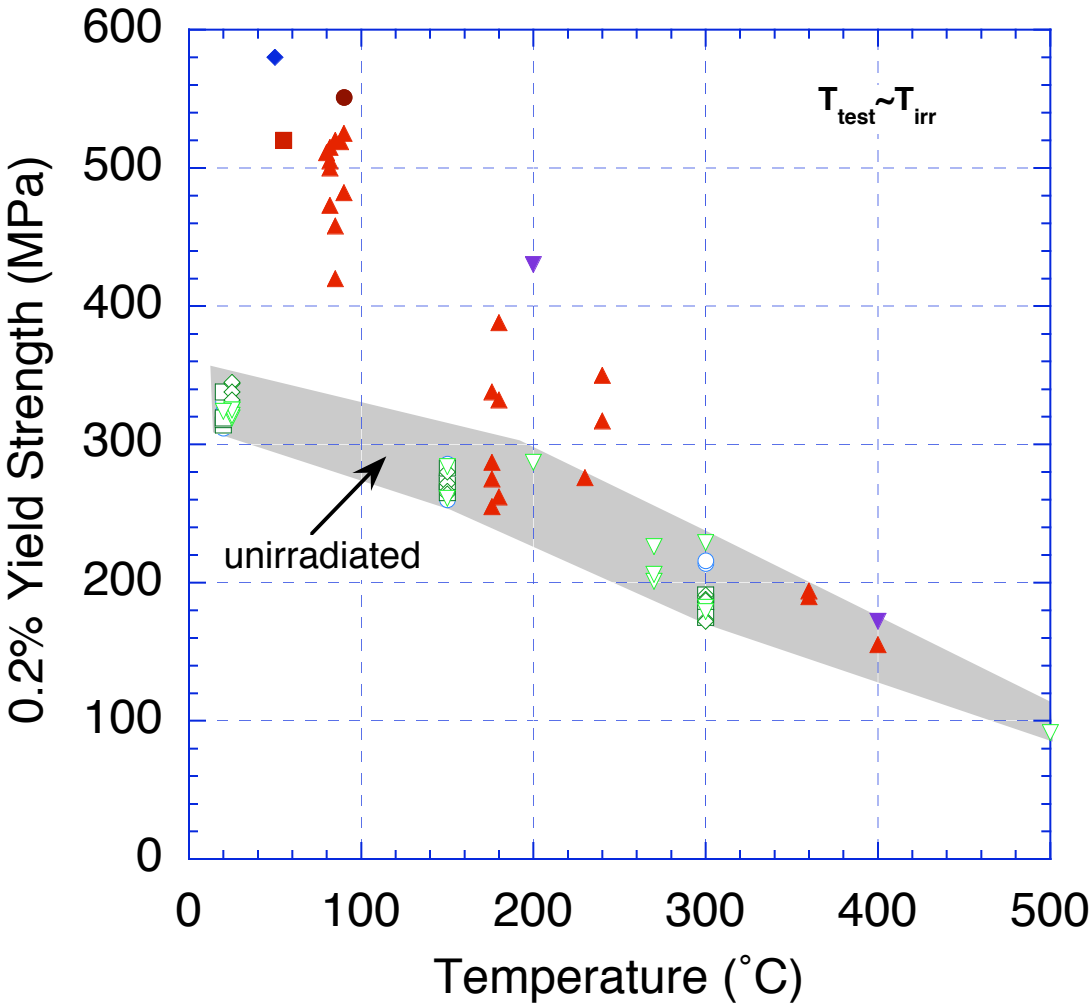

Fig. 2. Temperature dependence of yield strength in unirradiated and neutron irradiated GlidCop AL25 oxide dispersion strengthened copper [26,78,79].

metals above ~0.3 T_M. At these higher irradiation temperatures, rapid coarsening of the vacancy and interstitial defect cluster microstructure with increasing irradiation temperature is observed [32,36]. For FCC metals, the dominant defect clusters in the low-temperature radiation hardening regime are generally either vacancy-type stacking fault tetrahedra or a mixture of vacancy- and interstitial-type dislocation loops. For BCC metals, a significant hardening contribution is deduced to be associated with submicroscopic

cavities; interstitial-type dislocation loops also make a significant contribution. The radiation hardening behavior of neutron-irradiated austenitic stainless steel is particularly noteworthy because it exhibits a nonmonotonic temperature dependence. The tensile strength of stainless steel irradiated to moderate damage levels (above ~3 dpa) exhibits a maximum value at irradiation temperatures near 300˚C [28,77,80-82]. The microstructure at these conditions consists of a mixture of faulted dislocation loops, “black spot” defect clusters, and nanometer-sized cavities [83].

It has been suggested that dislocation channeling may also induce grain boundary cracking in some irradiated BCC alloys [38]. At higher temperatures, channel fracture has been observed in the grain interiors of some irradiated and deformed metals containing a high concentration of voids [84].

4. Comparison between tensile behavior and fracture toughness

One major consequence of dislocation channeling is that the associated extreme localization in the deformation within the cleared channels produces a very low macroscopic value for the uniform elongation as measured in a uniaxial tensile test [2,51,54]. Uniform elongations below 1% are commonly observed in both BCC and FCC metals irradiated at low temperatures. Although low values of uniform elongation can impose significant impacts on structural design criteria, low tensile elongation (and/or low tensile toughness) is not universally associated with low fracture toughness. The term "low temperature radiation embrittlement" dates back to the 1950s, and was originally associated with the low uniform elongation commonly observed in tensile tests of irradiated metals. Fracture toughness tests were performed infrequently on irradiated materials during this time period. Therefore, accurate comparisons between tensile behavior and fracture toughness of irradiated metals were virtually nonexistent (although low temperature irradiation was known to often produce significant reductions in fracture toughness, particularly in BCC alloys). In many cases, the pronounced decrease in uniform elongation in metals irradiated at low temperatures is not accompanied by comparable dramatic reductions in total elongation or reduction in area. Unfortunately, there is widespread association of the term “low temperature radiation embrittlement” to describe the behavior of irradiated metals with low uniform elongation.

There are many examples where low temperature radiation causes a simultaneous reduction in the uniform elongation (and also the tensile toughness, defined as the integrated area under the stress vs. strain tensile curve) and fracture toughness. However, radiation-induced reductions in uniform elongation and tensile toughness cannot be universally correlated with changes in fracture toughness (due to the importance of stress concentrators and prompt crack propagation effects in fracture toughness measurements). As outlined below, there are several recent examples in BCC and FCC alloys where tensile toughness and uniform elongation behavior has been explicitly shown to not correlate with fracture toughness.

Figure 3 compares the tensile and fracture toughness behavior of CuCrZr before and after irradiation [85,86]. Large reductions in uniform elongation and tensile toughness occur after irradiation to 0.3 dpa at ~50 and 200˚C (irradiated $e_u \leq 1\%$), whereas there was no change in the fracture toughness (K_J~150 MPa-m$^{1/2}$ before and after irradiation). Similarly, pronounced reductions in uniform elongation (irradiated $e_u \leq 1\%$) and tensile toughness have been observed in austenitic stainless steel irradiated to ~2 to 7 dpa at 225-330˚C [28,77,80-82]. However, high fracture toughness (K_J>150 MPa-m$^{1/2}$) is maintained in several heats of irradiated austenitic stainless steel even when the uniform elongation is low [80,87].

Figure 4 summarizes the tensile and fracture toughness behavior for two ferritic-martensitic steels irradiated to 2-3 dpa at low temperatures [87,88]. The tensile curves for HT-9 show significantly *higher* uniform elongations and *higher* work hardening capacity than the corresponding curves for F82H. The tensile toughness for HT-9 irradiated at 250˚C is about a factor of two *higher* than that for irradiated F82H. In contrast, the fracture toughness of irradiated HT-9 is significantly *lower* than that of irradiated F82H. The highest tensile toughness was observed for HT-9 irradiated at 250˚C and tensile tested at 90˚C; this set of experimental conditions produced the lowest fracture toughness (lower shelf behavior) in the corresponding fracture toughness tests. Similar differences in the qualitative trends for tensile and fracture toughness have been observed in V-4Cr-4Ti alloys [12,13,89]. For example, the uniform elongation and tensile toughness of V-4Cr-4Ti irradiated to 4 dpa at 400˚C *increased* by more than a factor of two as the test temperature was decreased from 400˚C to room temperature, whereas the fracture

toughness *decreased* by nearly an order of magnitude. Due to the lack of stress concentrators in the smooth tensile tests, it is clearly apparent that tensile toughness and/or uniform elongation is not a reliable quantitative or qualitative indicator of fracture toughness behavior.

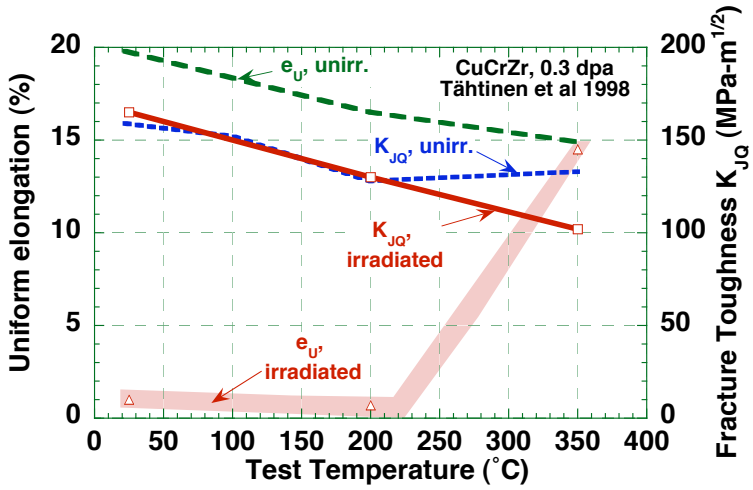

Fig. 3. Comparison of the uniform elongation and fracture toughness of CuCrZr before and after irradiation to 0.3 dpa, T_{test}~T_{irr} [85].

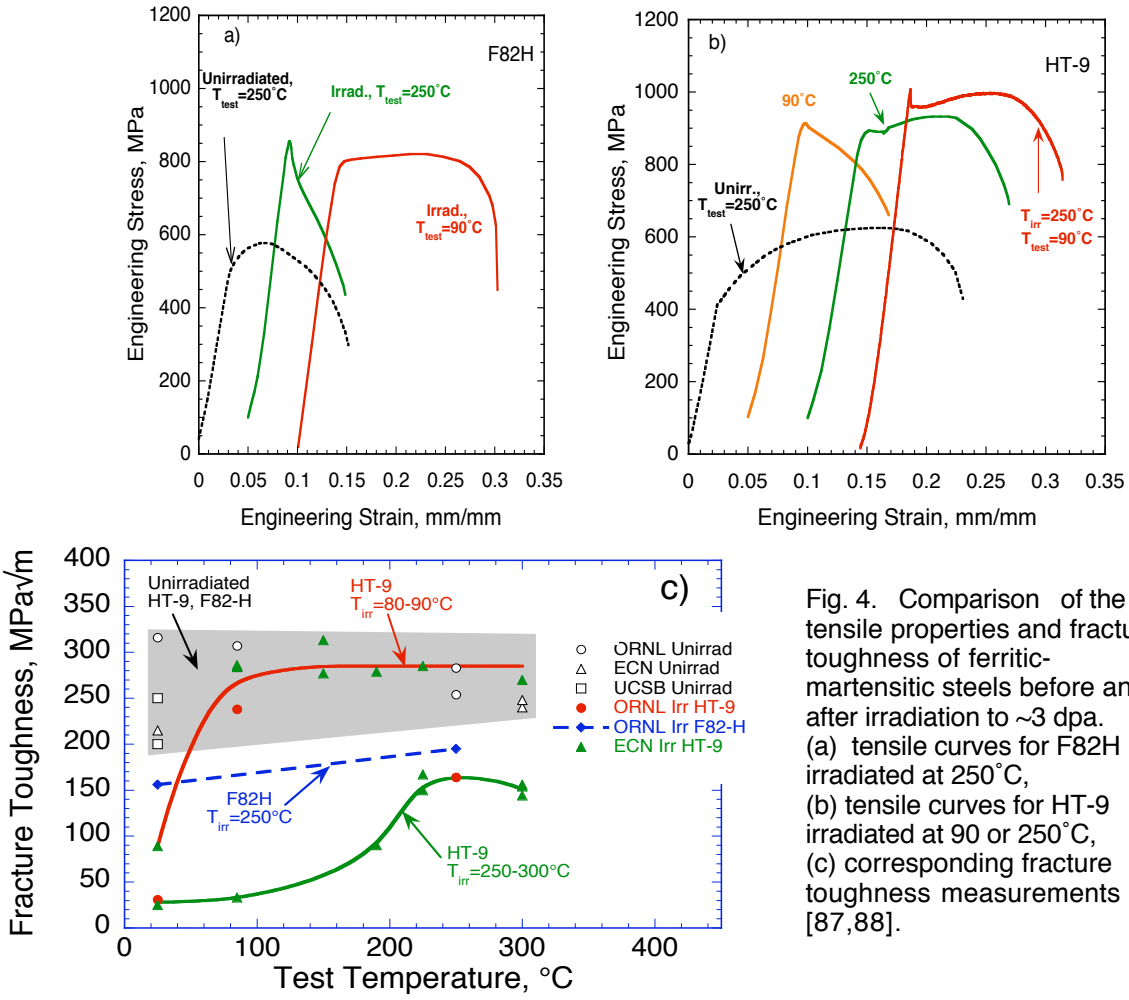

Fig. 4. Comparison of the tensile properties and fracture toughness of ferritic-martensitic steels before and after irradiation to ~3 dpa. (a) tensile curves for F82H irradiated at 250˚C, (b) tensile curves for HT-9 irradiated at 90 or 250˚C, (c) corresponding fracture toughness measurements [87,88].

5. Deformation maps for unirradiated and irradiated metals

5.1. Unirradiated deformation maps.

As outlined by Ashby [18], at least six different deformation mechanisms can be distinguished which produce permanent plastic deformation in metals: 1. In the absence of any defects, plastic deformation is induced when the stress exceeds the *theoretical shear strength*, which has a value of ~0.04μ. 2. The presence of dislocations in metals enables deformation to occur at stresses well below the theoretical shear stress. The stress required to induce *dislocation glide* is dependent on the spacing and strength of the microstructural obstacles (precipitates, solute atoms, etc.), and occurs via a thermally activated process. 3. *Twinning* occurs predominantly at low temperatures and moderate stresses. 4. Diffusional creep of atoms along grain boundaries (*Coble creep*) is important at moderate stresses and temperatures, particularly in fine-grained materials. 5. Diffusional creep via vacancy self-diffusion in the grain interior (*Nabarro-Herring creep*) becomes significant at very high temperatures. 6. At elevated temperatures and stresses, *dislocation creep* (power law creep) occurs by a process of dislocation climb and glide that is dependent on the vacancy self-diffusion coefficient and has a superlinear stress dependence, resulting in a cellular deformation structure. As in Ashby's original paper on deformation maps [18], we have ignored several other creep deformation mechanisms (in particular diffusional creep via pipe diffusion and Harper-Dorn creep [90]) in the present analysis in order to maintain readability of the deformation maps.

The strain rates for these 6 different deformation mechanisms are given by the following constitutive equations.

Ultimate shear strength

$$\dot{\gamma}_1 = \quad , \qquad \tau \geq 0.04\mu \tag{3a}$$

$$\dot{\gamma}_1 = 0, \qquad \tau < 0.04\mu \tag{3b}$$

Dislocation glide

$$\dot{\gamma}_2 = \dot{\gamma}_0 \exp\left[\frac{[H_0 - V(\tau - \tau_0)]}{kT}\right] \qquad \tau > \tau_0 \tag{4a}$$

$$\dot{\gamma}_2 = 0, \qquad \tau < \tau_0 \tag{4b}$$

where H_0 is the interaction enthalpy between glide dislocations and microstructural obstacles, b is the glide dislocation Burgers vector, k is Boltzmann's constant, T is the absolute temperature, and τ_0 is the athermal part of the flow stress [18,91,92]. The activation volume for dislocation glide is given by V~bdl, where l is the obstacle spacing on the glide plane and d is the obstacle size. The value for the pre-exponential constant for dislocation glide was assumed to be $\dot{\gamma}_0 = 10^6$ s^{-1} for all calculations. The key microstructural parameters for dislocation glide (H_0 and V) can be experimentally obtained from the temperature dependence of the flow stress at different strain rates. From equation 4, the dislocation glide flow stress is given by τ_0+H_0/V at absolute zero, and it equals τ_0 (athermal flow stress) at high temperatures. For this report, τ_0 is assumed to be constant although it is recognized that a temperature-dependence similar to that for the shear modulus would be more appropriate.

For BCC metals such as vanadium and ferritic steel, the lattice resistance associated with directional bonding (Peierls forces) has a strong impact on the dislocation glide behavior at low temperatures. Since the Peierls barrier represents a strengthening contribution rather than a deformation mechanism, its impact on the dislocation glide regime is handled by superposition of stresses instead of strain rates [18]. A linear superposition of the obstacle and Peierls stresses was assumed for this report (by modifying the low temperature glide stress component, H_0/V). In general, the nature of the various dislocation glide obstacles must be considered in order to determine the appropriate superposition relation. For example, short range obstacles would be expected to contribute as the square root of the sum of the squares of the Peierls and solute hardening components (quadratic superposition), whereas linear superposition is appropriate for the superposition of long range obstacles (e.g., coherent precipitates) and Peierls hardening [4,6,40].

The constitutive equations for deformation twinning are not firmly established [93], although there is evidence that the critical stress for twinning decreases with increasing strain rate and increases slowly with test temperature (both of which suggest that twinning is not a thermally activated process). For the present study, we have adopted a simplified version of the Venables model, where the twinning stress (σ_{tw}) is constant for a given material (except for the slight temperature dependence of the stacking fault energy, γ_{SF}):

$$\sigma_{tw} = 2\frac{\gamma_{SF}}{b} \tag{5a}$$

The following simple constitutive equation for twinning was assumed for the purpose of constructing the deformation maps, where it was assumed C_0=1 s^{-1} and $\dot{\varepsilon}_3$=0 for $\sigma < \sigma_{tw}$.

$$\dot{\varepsilon}_3 = C_0 \frac{\sigma - \sigma_{tw}}{\sigma} \qquad \sigma > \sigma_{tw} \tag{5b}$$

The constitutive equation for diffusional creep is given by [90]

$$\dot{\varepsilon}_{4,5} = \frac{30\Omega\sigma}{kTL^2}\left[D_{SD} + \frac{2\pi D_B b(\sigma - \sigma_1)}{L\sigma} + C_1 D_P \rho_d b^2\right] \tag{6}$$

where Ω is the atomic volume ($a_0^3/4$ for FCC, $a_0^3/2$ for BCC) L is the grain diameter, D_{SD}, D_B and D_P are the diffusion coefficients associated with self-, grain boundary- and pipe dislocation-diffusion, respectively, ρ_d is the dislocation density, and C_1 is a constant of order unity. In this equation, the first term inside the brackets is associated with *Nabarro-Herring creep*, the second term is associated with *Coble creep*, and the third term (which is ignored for the present analysis) is associated with dislocation pipe diffusion [90]. Since the dislocation density in deformed specimens is proportional to the square of the applied stress [90,94], diffusional creep via pipe diffusion can be of particular importance at higher stress levels, and is responsible for a superlinear (cubic) dependence of diffusional creep on applied stress. Although diffusional creep via pipe diffusion was not included in the present analysis for sake of simplicity, it should be included in any detailed analysis of creep mechanisms. We have included a grain boundary friction stress (σ_1) in eqn. (6) to account for the minimum stress needed to unpin grain boundaries from particles during creep deformation. A more accurate representation would also involve computing the maximum velocity that particles can be dragged by grain boundaries [95]. Previous work [96] has reported that the grain boundary frictional stress can be described by the following functional dependence: $\sigma_1 = C_2(1-T/T_M)$, where C_2 is the frictional stress at zero kelvin.

The constitutive equation for diffusion-controlled dislocation creep (power law creep) is given by [90,94]

$$\dot{\varepsilon}_6 = \frac{A\Omega b}{kT}\left[D_{SD} + 200 D_P \left(\frac{\sigma - \sigma_2}{\sigma}\right)^2\right]\left(\frac{\sigma - \sigma_2}{\sigma}\right)^n \qquad \sigma \geq \sigma_2 \tag{7a}$$

$$\dot{\varepsilon}_6 = 0, \qquad \sigma < \sigma_2 \tag{7b}$$

where the dimensionless constant A~10^9 and the power law exponent is n~5 [94] and σ_2 is the dislocation friction stress associated with solute or other dislocation obstacles (e.g., precipitates). Power law creep thereby gives rise to stress exponents of 5 to 7 depending on the relative importance of self-diffusion and

dislocation pipe diffusion. Alternative expressions for creep of alloys containing dispersed precipitates have also been developed [90,97], but will not be considered in the present analysis for sake of simplicity.

The relevant materials data used for the deformation calculations on copper alloys, Type 316 austenitic stainless steel, V-4Cr-4Ti, and 8-12%Cr ferritic/martensitic steel are summarized in Table 1 [18,94,98-109]. Due to a lack of data, the stacking fault energy was assumed to be constant for all materials except 316 stainless steel, where experimental data suggest the temperature coefficient is 0.00003 J/m^2-K [107]. There is considerable variability in the literature regarding dislocation creep constitutive equations and associated creep constants. We have adopted the recommendations by Sherby and Miller [94] in our calculations as opposed to the values contained in the original Ashby map paper [18]. Following the method outlined by Ashby [18], the stress and temperature regimes where a particular deformation mechanism is dominant was determined from calculations of the deformation rates given by equations 3-7 over a wide range of stresses and temperatures. The boundary between two deformation fields corresponds to the stress-temperature conditions where both processes contribute equally to the plastic strain rate. In most of the figures to be presented, the boundary between elastic behavior and the various plastic deformation fields was drawn for an arbitrary plastic strain rate of 10^{-8} s^{-1}. The elastic-plastic boundary (and the boundaries between the plastic deformation fields) for other strain rates can be readily determined with equations 3-7. It should be noted that there is significant uncertainty in several of the materials parameters used for the deformation map calculations. For example, the variability in the reported grain boundary diffusion energy is nearly a factor of two for several material systems [99,110]. This causes a corresponding significant uncertainty in the quantitative values for the deformation maps. Detailed analyses of experimental thermal creep data are needed to determine these fundamental materials parameters, and to confirm the extent of the different thermal creep mechanism regimes.

Table 1. Summary of materials parameters used in the Ashby deformation map calculations [18,98-109]. A constant value of $A=1x10^9$ [94] was used for the dislocation creep constant (eqn. 7a) for all materials.

Alloy	Burgers vector (nm)	T_M (K)	Shear modulus at 300 K (GPa)	$1/\mu$ $d\mu/dT$ (10^{-4}/K)	Stacking fault energy at 300 K (J/m^2)	D_0 for bulk diffusion (10^{-4} m^2/s)	Bulk diffusion activation energy (kJ/mol)	D_0 for g.b. diffusion (10^{-4} m^2/s)	g.b. diffusion activation energy (kJ/mol)	D_0 for pipe diffusion (10^{-4} m^2/s)	Pipe diffusion activation energy (kJ/mol)
Cu-Al_2O_3 CuNiBe	0.256	1356	44.7 [98]	-3.8 [98]	0.055 [106]	0.6 [99]	200 [99,100]	0.1 [18]	100 [18,99]	0.04 [99]	148 [99]
316 SS	0.258	1650	77 [101]	-3.9 [101]	0.03 [106,107]	0.4 [100]	280 [100]	0.1 [18]	150	0.1	190
V-4Cr-4Ti	0.262	2175	46 [102]	-1.7 [103]	0.2 [108]	0.3 [100]	300 [100,104]	1.0 [18]	160	0.1	230
Fe-8Cr-2WVTa	0.248	1800	84 [105]	-2.3 [105]	0.2 [109]	1.0 [100]	260 [100,104]	1.0 [18]	150	0.1	210

Figures 5-11 show the calculated deformation maps for the four classes of unirradiated materials. The right hand axes show the uniaxial tensile stresses for equiaxed polycrystalline materials, which were obtained by multiplying the shear stress by the Taylor factor (3.06). Most of the deformation maps were calculated for a elastic-plastic boundary strain rate of 10^{-8} s^{-1}, which is a common deformation rate for experimental studies (equivalent to ~30%/year plastic deformation). One example of a higher strain rate deformation map is given to illustrate the strong effect of strain rate on the location and extent of the various deformation mode regimes. The internal boundaries for the deformation maps were calculated by determining the conditions for equal strain rate by competing mechanisms (corresponding strain rates are much higher than the elastic-plastic boundary strain rate). The dominant deformation mode at low temperatures and moderate stresses (greater than or equal to the yield stress) is dislocation glide. Twinning was not calculated to occur in any of the unirradiated materials except for Type 316 SS at very low temperatures. Diffusional creep (Coble creep, Nabarro-Herring creep) dominates at high temperatures and low stresses, particularly in fine-grained materials. Dislocation (power law) creep is dominant at moderate stresses (typically 20-100% of the yield stress) at temperatures above ~0.4 T_M.

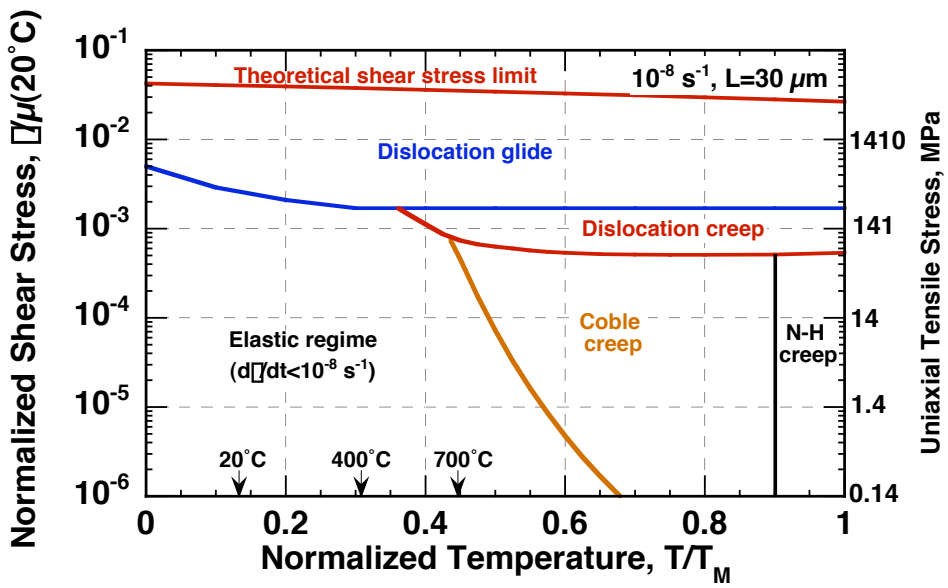

Fig. 5. Deformation map for V-4Cr-4Ti at a plastic strain rate of 10^{-8} s^{-1}. The map was constructed assuming τ_0=90 MPa, H_0=1.5 eV, V=100 b^3, τ_i=0 and τ_2=15 MPa.

Figures 5 and 6 compare the calculated deformation maps for V-4Cr-4Ti at a strain rate of 10^{-8} and 10^{-4} s^{-1}, respectively. The grain size was taken to be 30 μm for the calculations; typical grain sizes in published V-4Cr-4Ti studies range from 18 to 35 μm. In both of these figures the assumed value for the grain boundary friction stress was τ_i=0 and the value of the solute and precipitate friction stress was taken to be τ_2=15 MPa (independent of temperature). The assumption of zero grain boundary friction stress causes the Coble creep regime to extend to unrealistically low stresses at temperatures above 800˚C; a more accurate calculation in this temperature range should use a nonzero value for τ_i, although the quantitative magnitude of τ_i for V-4Cr-4Ti is uncertain. It is worth noting that twinning is not predicted to occur at any conditions for the values assumed in Table 1, whereas twinning has been experimentally observed in vanadium deformed at low temperature [111]. This implies that the stacking fault energy for the {112} slip plane may be less than 0.2 J/m^2. The calculated deformation map indicates that both Coble creep and dislocation creep will have significant contributions at 10^{-8} s^{-1} for temperatures of 700-800˚C and uniaxial

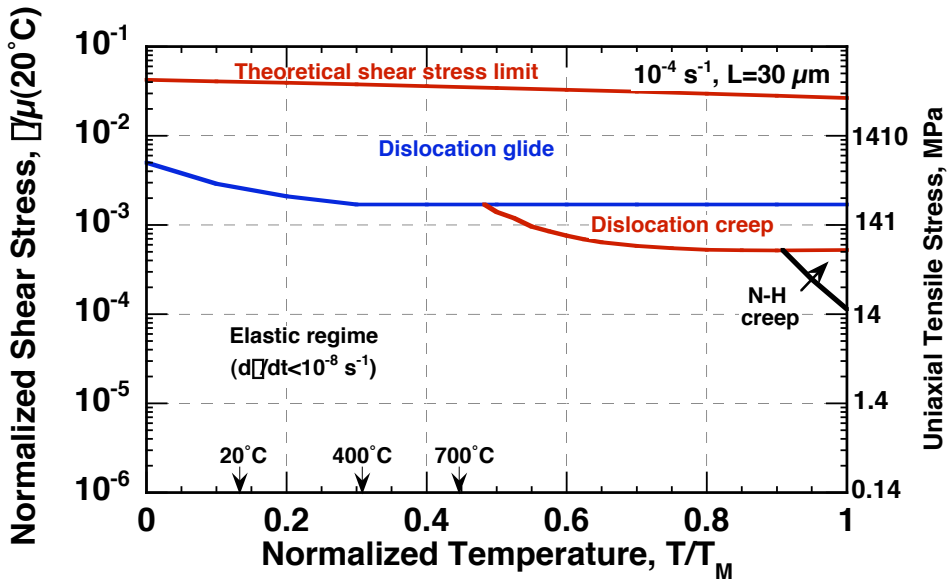

Fig. 6. Deformation map for V-4Cr-4Ti at a plastic strain rate of 10^{-4} s^{-1}. The map was constructed assuming τ_0=90 MPa, H_0=1.5 eV, V=100 b^3, τ_i=0 and τ_2=15 MPa

.
tensile stresses of 50-120 MPa. Therefore, detailed analyses of the creep behavior at these conditions are necessary in order to separate the contributions associated with these two creep mechanisms (stress

dependence and controlling activation energy). It is also apparent from the calculated V-4Cr-4Ti creep deformation map (Fig. 5) that the dominant creep deformation mode at moderate temperatures (~600˚C) will likely be different from the deformation mode at temperatures above 650˚C. Therefore, a simplistic application of Larson-Miller correlation plots should not be used to extrapolate thermal creep results to temperatures or strain rates (test times) significantly outside the experimental regime where data were acquired [18,90,91]. The main impact of increasing the strain rate from 10^{-8} to 10^{-4} s^{-1} is to shift the creep regime to higher temperatures and stresses. In addition, the Coble creep deformation regime does not exist in V-4Cr-4Ti for the higher strain rate condition. The calculations suggest that a straightforward experimental determination of the dislocation power law creep parameters for V-4Cr-4Ti may be obtained at strain rates of ~10^{-4} s^{-1} and temperatures of 700-900˚C, since Coble creep would not have a significant influence at any temperature or stress and Nabarro-Herring creep is insignificant for temperatures up to ~1500˚C. Recently, V-4Cr-4Ti thermal creep and tensile data at a wide range of strain rates have been acquired under uniaxial tensile conditions in vacuum [112-114] and under biaxial stress conditions in vacuum [115] and lithium [116]. The experimental data will be compared with the calculated deformation map results in a future contribution in order to confirm the values of several of the material variables used in the calculation.

Figure 7 shows the calculated deformation map for Fe-8Cr-2WVTa (F82H ferritic-martensitic steel) at a strain rate of 10^{-8} s^{-1}. The assumed value for the grain boundary friction stress was τ_1=0 and the value of the solute and precipitate friction stress was taken to be τ_2=20 MPa. The grain size of the original heat of F82H (22 μm) was used for the calculation; larger grained heats of F82H and other reduced-activation ferritic-martensitic steels have also been fabricated. Since the martensitic phase is unstable at high temperatures, the parameters used for the ferritic-martensitic steel Ashby deformation map restricts the validity of the calculation to temperatures below ~0.6 T_M. The dislocation glide stress boundary decreases rapidly at temperatures above 0.5 T_M due to age-softening of the tempered martensitic structure; for the purposes of the deformation map calculation, it was assumed that the dislocation glide stress decreased by a factor of about three due to age-softening near 700˚C. The calculated deformation map for a plastic strain rate of 10^{-8} s^{-1} indicates that deformation of F82H is

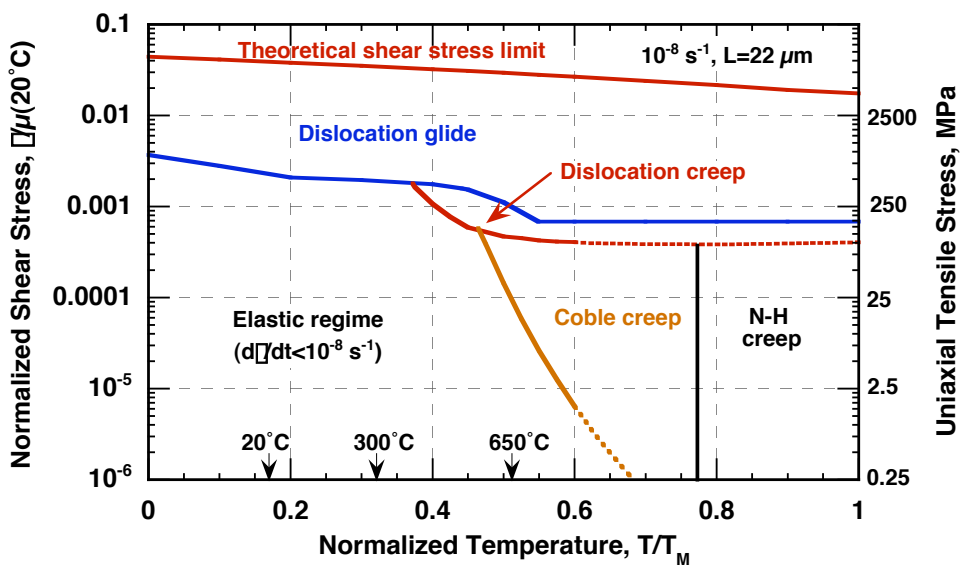

Fig. 7. Deformation map for Fe-8Cr-2WVTa at a plastic strain rate of 10^{-8} s^{-1}. The map was constructed assuming τ_0=170 MPa, H_0=1.5 eV, V=100 b^3, τ_1=0 and t_2=20 MPa. Dashed lines are used for temperatures above 0.6 T_M due to a phase change.

controlled by dislocation (power law) creep at temperatures above ~450˚C (~0.4 T_M), and by Coble creep at temperatures above ~0.5 T_M. The extent of the Coble creep regime to low stresses is somewhat exaggerated in Fig. 7 due to the assumption of a grain boundary friction stress of τ_1=0. Inclusion of a nonzero grain boundary friction stress would significantly reduce the extent of the Coble creep regime (see example for GlidCop dispersion strengthened copper presented in Figs. 8-9 later in this section). Coble creep is also calculated to be negligible for ferritic-martensitic steels with grain size >40 μm. In the absence of Coble creep, Nabarro-Herring creep is predicted to become significant at 10^{-8} s^{-1} for temperatures above ~750˚C. It should be noted that dislocation creep can be suppressed by microstructural changes (which increase τ_2). This may be the basis for the impressive creep strengths of

oxide dispersion strengthened (ODS) ferritic steels at temperatures above 550˚C [117,118]. For example, the reported 1000 h creep rupture strength for ODS Fe-12Cr steel [117] at 650˚C was about three times higher than that for F82H [105]. Deformation map calculations for ODS ferritic steel (not shown) using the F82H material parameters in Table 1 and a grain size of 50 μm suggest that the upper temperature limit for structural applications of ODS steel may be as high as ~850˚C (temperature limit determined by Nabarro-Herring creep). Recent thermal creep tests on nanocomposited ODS steels [118] have observed good creep strength for temperatures in excess of 800˚C, in agreement with this calculation.

Figures 8 and 9 compare the calculated deformation maps for oxide dispersion strengthened copper at a strain rate of 10^{-8} for a dispersoid friction stress of τ_2=15 MPa and a grain boundary friction stress of τ_1=0 and 10(1-T/T_M) MPa, respectively. The latter grain boundary friction stress value was reported for oxide dispersion strengthened copper [96]. The grain size was taken to be 5 μm, which is intermediate between the grain size in the short transverse (<1 μm) and longitudinal (~10 μm) directions for GlidCop Al25 oxide dispersion strengthened copper. The relatively small grain size in GlidCop Al25 causes the calculated Coble creep to become significant for temperatures as low as 200˚C (~0.35 T_M) at this strain rate. Since the oxide dispersion does not significantly influence the grain boundary sliding behavior, the potential high-temperature strength benefits associated with the oxide particles are not achieved in GlidCop Al25. The low strength of GlidCop Al25 (compared to larger-grained Cu alloys such as CuCrZr) is observable at elevated temperatures (400-600˚C) even for normal tensile test strain rates of ~10^{-3} s^{-1} [79,119-121]. The deformation map analysis suggests that significant improvement in the elevated temperature strength of GlidCop could be achieved if the manufacturing process could be altered to create a larger grain size.

The assumption of zero grain boundary friction stress (τ_1=0) in Fig. 8 produces high thermal creep at exceedingly small stresses (<1 MPa) at temperatures above 400˚C, in disagreement with the existing literature data. The inclusion of a frictional stress of τ_1 = 10(1-T/T_M) MPa in Fig. 9 produces fair agreement between the calculated and experimental [78,122] creep of dispersion strengthened copper at 300-600˚C. The dominant creep deformation mechanism is predicted in Fig. 9 to change from Coble to Nabarro-Herring creep at a temperature near 500˚C.

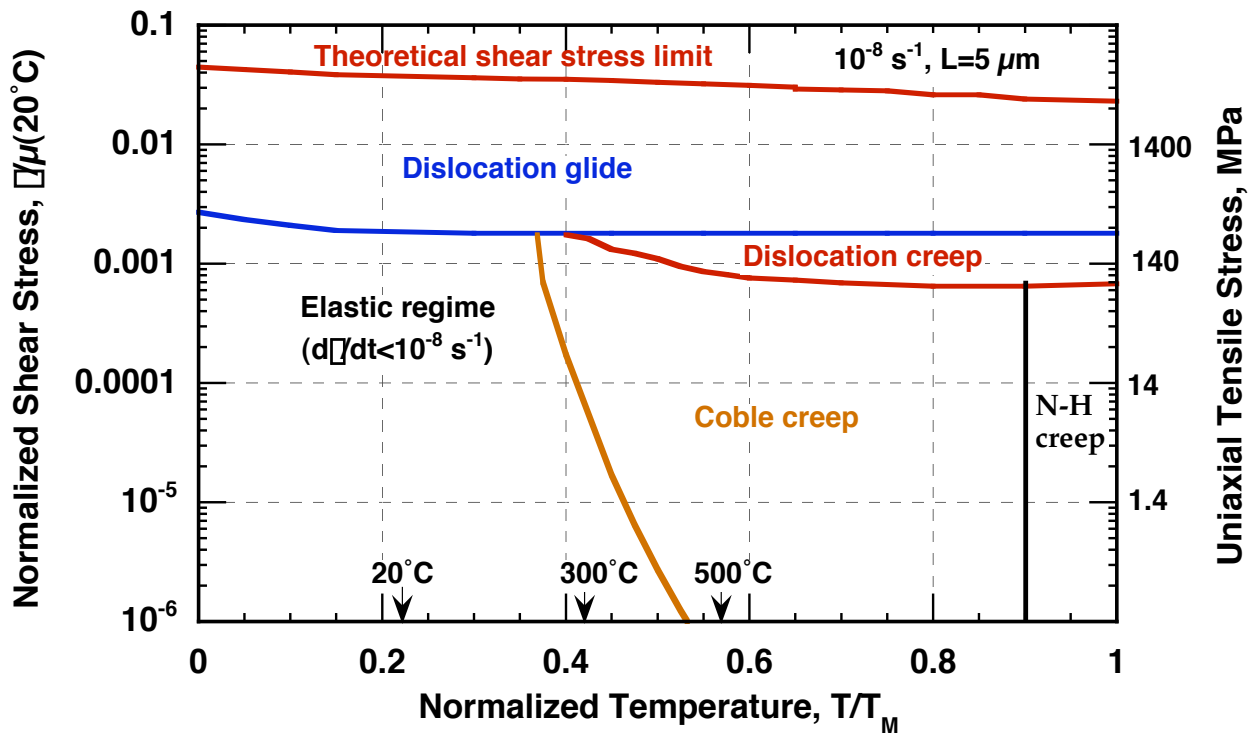

Fig. 8. Deformation map for oxide dispersion strengthened copper (GlidCop Al25) at a plastic strain rate of 10^{-8} s^{-1}. The map was constructed assuming τ_0=80 MPa, H_0=1.0 eV, V=200 b^3, τ_1=0 and τ_2=15 MPa.

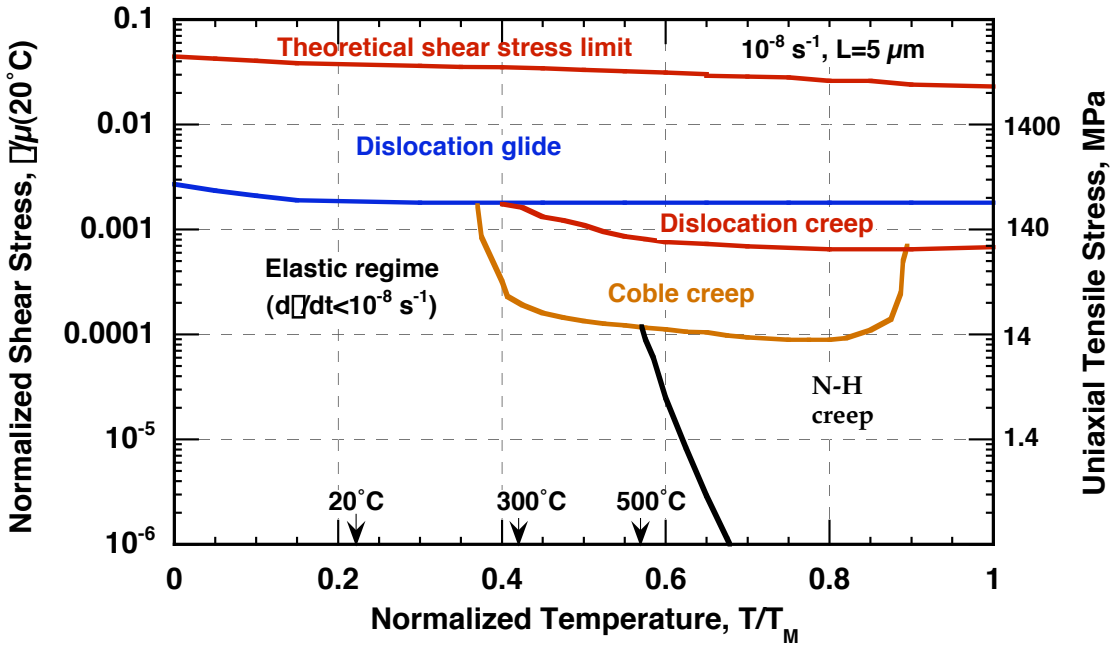

Fig. 9. Deformation map for oxide dispersion strengthened copper (GlidCop Al25) at a plastic strain rate of 10^{-8} s^{-1}. The map was constructed assuming τ_i = 10(1-T/T$_M$) MPa and τ_2=15 MPa.

The deformation map for high-strength CuNiBe at a strain rate of 10^{-8} s^{-1} is summarized in Fig. 10, based on a grain size of 30 μm, a precipitate friction stress of τ_2=35 MPa and a grain boundary friction stress of τ_1=0. Dislocation (power law) creep is calculated to be the controlling plastic deformation mechanism in CuNiBe at temperatures from ~180˚C to ~400˚C at this strain rate. Coble creep is calculated to become the controlling plastic deformation process in this alloy at moderate stresses and elevated temperatures (T>400˚C). An examination of the fracture surfaces of CuNiBe specimens tensile tested at 20 to 500˚C has found a transition to ductile intergranular fracture at temperatures above 400˚C [119,123], in qualitative agreement with the calculated transition to Coble creep in this temperature range.

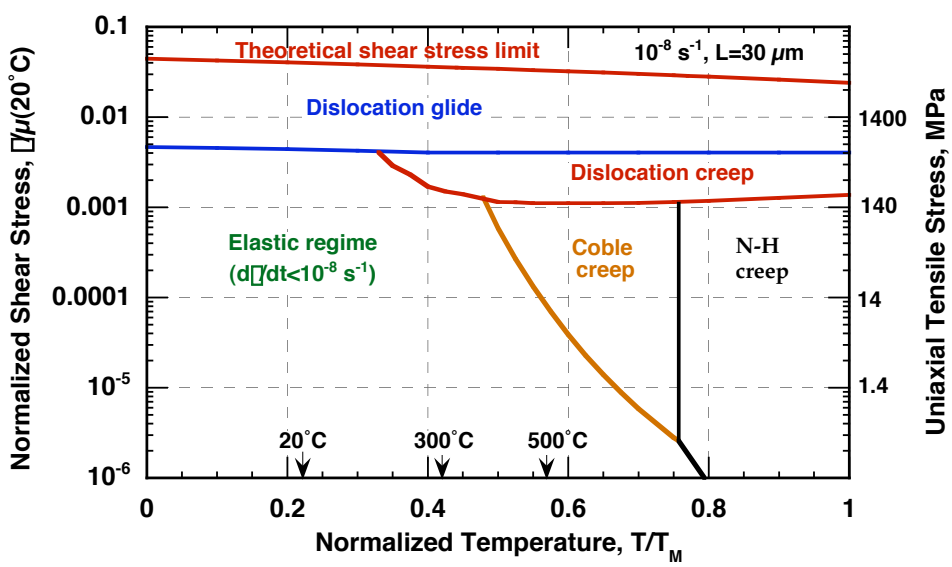

Fig. 10. Deformation map for precipitation-strengthened CuNiBe (Brush-Wellman Hycon 3HP) at a plastic strain rate of 10^{-8} s^{-1}. The map was constructed assuming τ_0=180 MPa, H$_0$=0.8 eV, V=150 b^3, τ_1=0 and τ_2=35 MPa.

Figure 11 shows the calculated deformation map for Type 316 austenitic stainless steel at a strain rate of 10^{-8} s^{-1}. The assumed value for the grain boundary friction stress was τ_1=0 and the value of the solute and precipitate friction stress was taken to be τ_2=15 MPa. A grain size of 50 μm was used for the calculation. A very limited twinning regime occurs at temperatures near absolute zero. Dislocation glide is the dominant deformation mechanism from low temperatures up to ~550˚C. Dislocation creep is the dominant creep mechanism for temperatures between ~550 and ~900˚C (0.7 T_M). A limited Coble creep regime occurs at temperatures above 900˚C, and Nabarro-Herring creep is the dominant deformation mechanism at temperatures above ~1050˚C. Due to the absence of Coble and Nabarro-Herring creep at intermediate temperatures, stainless steel retains relatively high strength up to ~650˚C even for strain rates of ~10^{-10} s^{-1}.

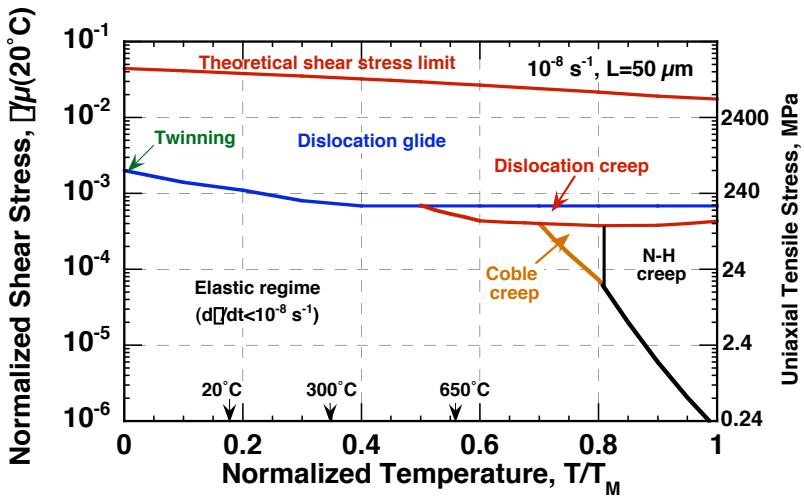

Fig. 11. Deformation map for Type 316 austenitic stainless steel at a plastic strain rate of 10^{-8} s^{-1}. The map was constructed assuming τ_0=60 MPa, H_0=1.6 eV, V=150 b^3, τ_1=0 and τ_2=15 MPa.

5.2. Irradiated deformation maps.

Irradiation causes several modifications to the unirradiated deformation behavior of metals and alloys. The main modifications can be classified as *radiation hardening*, *radiation-enhanced softening*, *irradiation creep*, and *high temperature He embrittlement*. Of these phenomena, only irradiation creep and high temperature He embrittlement represent new deformation mechanisms (as discussed later, some aspects of He embrittlement are similar to diffusional creep, but the stress dependence and activation energies may be different). The primary impact of radiation hardening and radiation-enhanced softening is a modification of the dislocation glide flow stress (τ_0) and dislocation creep frictional stress (τ_2).

As summarized in sections 2 and 3, increased resistance to dislocation glide (*radiation hardening*) typically occurs for irradiation temperatures below ~0.3 T_M due to the formation of a high density of defect clusters. This defect cluster hardening predominantly contributes to athermal stress term (τ_0) in equations 4a-4c. Radiation hardening can also modify the dislocation friction stress (τ_2) for dislocation (power law) creep, although the dislocation barriers produced by irradiation at intermediate elevated temperatures (0.3-0.6 T_M, where dislocation creep is significant) are generally of secondary importance compared to the unirradiated solute and precipitate friction stress. Since in most cases radiation hardening is associated with defect clusters with short range stress fields, we will assume quadratic superposition of the radiation hardening and unirradiated dislocation glide obstacle strengths: $\tau_0=(\tau_0^2(\text{unirr}) + \tau_0^2(\text{irr}))^{1/2}$, where τ_0(unirr) and τ_0(irr) are the dislocation glide athermal stresses associated with the obstacles in the unirradiated material and the radiation-produced defect clusters, respectively. One of the consequences of radiation hardening is that the requirement of higher stresses to activate dislocation glide (due to pinning of dislocations by radiation-induced defect clusters) can result in an expansion of the extent of the low-temperature twinning and intermediate-temperature dislocation creep regimes.

The phenomenon of dislocation channeling that is frequently observed in radiation hardened metals and alloys (cf. sections 2 and 3) can be regarded as a manifestation of dislocation glide, as opposed to a new deformation mechanism. Although the consequences of the localized deformation that occur with dislocation channeling can be profound, the fundamental mechanism is still associated with dislocation interaction with matrix obstacles. It should be noted that the strain rate dependence of radiation

hardening is often different compared to that for thermally-produced obstacles [1,26,30,66,124-126]. Therefore, the value of τ_0 and τ_2 at the appropriate strain rate should be used for the deformation map analysis. At intermediate temperatures, the phenomenon of void channel fracture has occasionally been observed [84]. This can also be considered to be a modification of dislocation glide deformation with localized flow.

At temperatures above ~0.5 T_M, *radiation-enhanced softening* is often observed in structural alloys (producing a decrease in τ_0 and τ_2) [13,28,29,78,127-129]. This softening can be included as a modification of the dislocation glide flow stress (τ_0) and dislocation creep frictional stress (τ_2).

The constitutive equation for the strain rate dependence of *irradiation creep* is given by

$$\tau_7 = 3.06(B_0 + D\dot{S})\tau P \qquad (8)$$

where P is the displacement rate (dpa/s) and B_0 is the creep compliance (~10^{-6} MPa^{-1} dpa^{-1} at intermediate temperatures of ~0.3-0.6 T_M for FCC alloys, and ~0.5x10^{-6} MPa^{-1} dpa^{-1} for BCC alloys) [71,72,130]. There is evidence that B_o increases at lower temperatures, which has been attributed to an extended transient dose regime due to the difference in mobility of vacancy and interstitial point defects at low temperatures [15,72,131]. This accelerated transient low temperature creep regime was ignored for the present analysis. Similarly, the potentially enhanced irradiation creep rate associated with formation of He bubbles at temperatures near 0.4 T_M [132] has been not included. At very low temperatures (below room temperature), irradiation creep is controlled by the interstitial diffusivity and the value of B_0 becomes very small. The creep-swelling coupling coefficient D has a value of ~0.006/MPa for both austenitic and ferritic steels [72]. The void swelling rate $\dot{S}$ in the void swelling regime (~0.3 to 0.6 T_M) has typical steady-state values of 0.5-1%/dpa for FCC alloys and ~0.05%/dpa for BCC alloys, although a recent reanalysis of experimental data suggests that steady state swelling rates for ferritic/martensitic steels may be as high as 0.25 to 0.5%/dpa [72]. The void swelling rate at doses below the transition to steady state swelling is typically ~0.01-0.05%/dpa. The temperature dependence of swelling at low and high temperatures can be described by approximate analytical expressions [133]. At low doses and strain rates, irradiation creep is a particularly important deformation mechanism for low to intermediate temperatures. At high doses, stress-assisted swelling may become the dominant deformation mode in FCC metals at intermediate temperatures (0.3-0.6 T_M) particularly if the transition to steady-state swelling occurs. However, in this case the material would likely be unacceptable for engineering structures due to the high volumetric swelling that would be introduced (swelling levels above 5% typically cannot be accommodated in the engineering design of structures). The projected impact of the creep-swelling mechanism is lower (but still important) in ferritic-martensitic steels and vanadium alloys due to their lower swelling rates compared to austenitic steels.

High temperature helium embrittlement is due to the migration of transmutation-produced helium to grain boundaries, producing helium-vacancy cavities that cause preferential deformation along grain boundaries [16,73,134]. The diffusion and nucleation of helium-vacancy cavities at grain boundaries is strongly enhanced by applied stress [134,135]. Since this phenomenon involves defect migration to grain boundaries, some aspects of high temperature He embrittlement are analogous to Coble and Nararro-Herring diffusional creep. It is well established that the stress dependence as well as the physical mechanisms that control the He embrittlement creep *rupture* temperature dependence are significantly different from diffusional and power-law creep [16,17,134,136]. However, existing experimental data generally do not show a significant effect of helium on the creep *rate* at temperatures near 0.5 T_M [71,136-138], and there are no known theoretical models that predict an effect of He on steady state creep. Unfortunately, much of the available experimental data on He embrittlement effects have been obtained at relatively high stresses and strain rates (tensile tests), which minimizes the influence of helium on deformation mechanisms. Two competing effects of helium on the steady state creep rate can be envisioned. First, the presence of helium-filled cavities in the matrix can increase the value of the solute and precipitate friction stress (τ_2) for dislocation power law creep. Conversely, helium migration to grain boundaries could significantly reduce the coble creep parameters for the grain boundary frictional stress (τ_1) and grain boundary diffusivity due to grain boundary cavity formation, causing grain boundary deformation and fracture to occur at very low stresses. Further work is needed to assess the importance of these competing mechanisms on the controlling deformation behavior of irradiated materials. In the present study, He embrittlement effects are not included in the deformation maps. Simplified models for

the effect of He on rupture time and rupture strain (fracture) are available [134], and will be briefly summarized in section 6.

The calculated deformation map at a strain rate of 10^{-8} s^{-1} for Type 316 stainless steel irradiated to a relatively low dose of 1 dpa at a dose rate of 10^{-6} dpa/s is given in Fig. 12. A grain size of 50 μm was used for the calculation. The assumed value for the grain boundary friction stress was τ_1=0 and the value of the solute and precipitate friction stress was taken to be τ_2=15 MPa (same values as for Fig. 11). There is some evidence that irradiation-induced defects may decrease the steady state creep rate of stainless steel at elevated temperatures (~650˚C) [136], possibly due to increasing the frictional stress τ_2. This possibility needs further investigation. The dislocation glide obstacle stress (τ_0) was fitted to temperature-dependent experimental radiation hardening data for stainless steel irradiated to ~1 dpa [77]. The main effect of irradiation at these conditions is to increase the flow stress for dislocation glide. This causes twinning to be the dominant deformation mode up to room temperature, and the dislocation creep regime is extended to lower temperature compared to the unirradiated case (cf. Fig. 11 and Fig. 12). The calculated deformation map for irradiated stainless steel is in agreement with experimental observations which have reported twinning following deformation near room temperature [65-68,139].

Irradiation creep is not predicted to be a significant deformation mechanism for the conditions used in the Fig. 12 calculation. On the other hand, irradiation creep is predicted to be significant at lower plastic strain rates (below 10^{-9} s^{-1}). Figure 13 shows the calculated deformation map at a strain rate of 10^{-10} s^{-1} (0.3%/year) for Type 316 stainless steel irradiated to 1 dpa at a dose rate of 10^{-6} dpa/s. All of the parameters except strain rate were identical for the calculations used to construct Figs. 12 and 13. A swelling rate of 0.05%/dpa was assumed for the temperature range 0.4-0.55 T_M (400-625˚C), and the swelling rate was assumed to decrease to zero at high and lower temperatures using a temperature-dependent relation outlined by Garner and Wolfer [133]. Two distinct irradiation creep regimes are discernable, corresponding to the two terms in Eqn. 8. At very low temperatures where vacancies are immobile (<300 K for stainless steel), irradiation creep becomes negligible due to low self-interstitial atom (SIA) mobility. An SIA migration energy of 24 kJ/mol (0.25 eV) was assumed for the calculation.

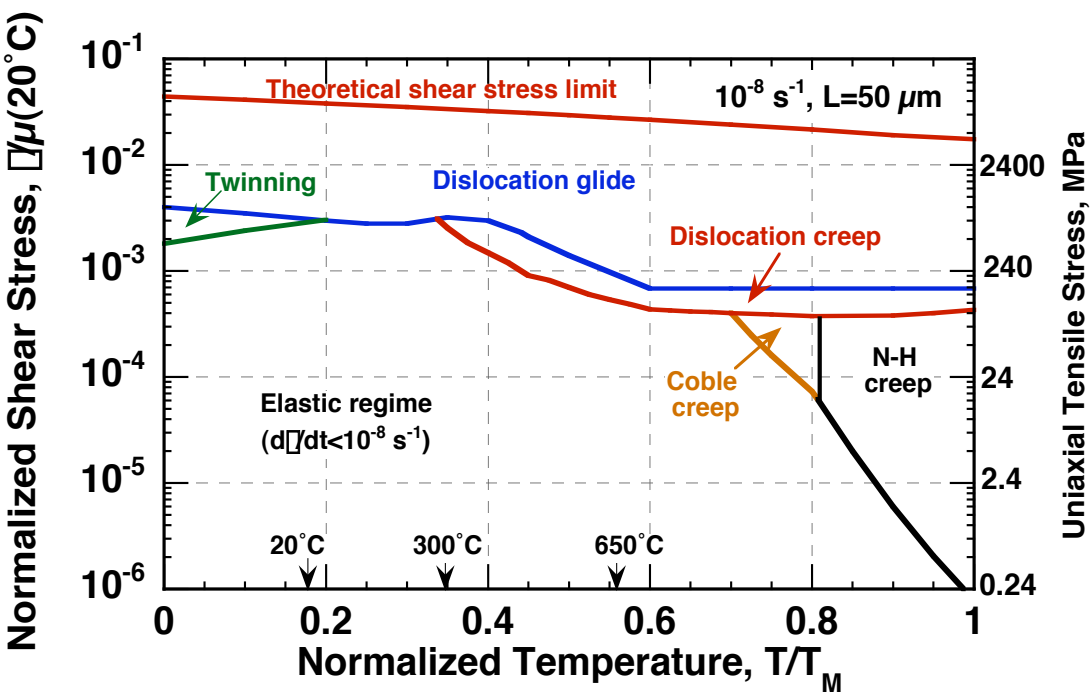

Fig. 12. Deformation map for Type 316 austenitic stainless steel irradiated to 1 dpa at 10^{-6} dpa/s for a plastic strain rate of 10^{-8} s^{-1}. The map was constructed assuming τ_0=240 MPa, H_0=1.0 eV, V=120 b^3, τ_1=0 and τ_2=15 MPa.

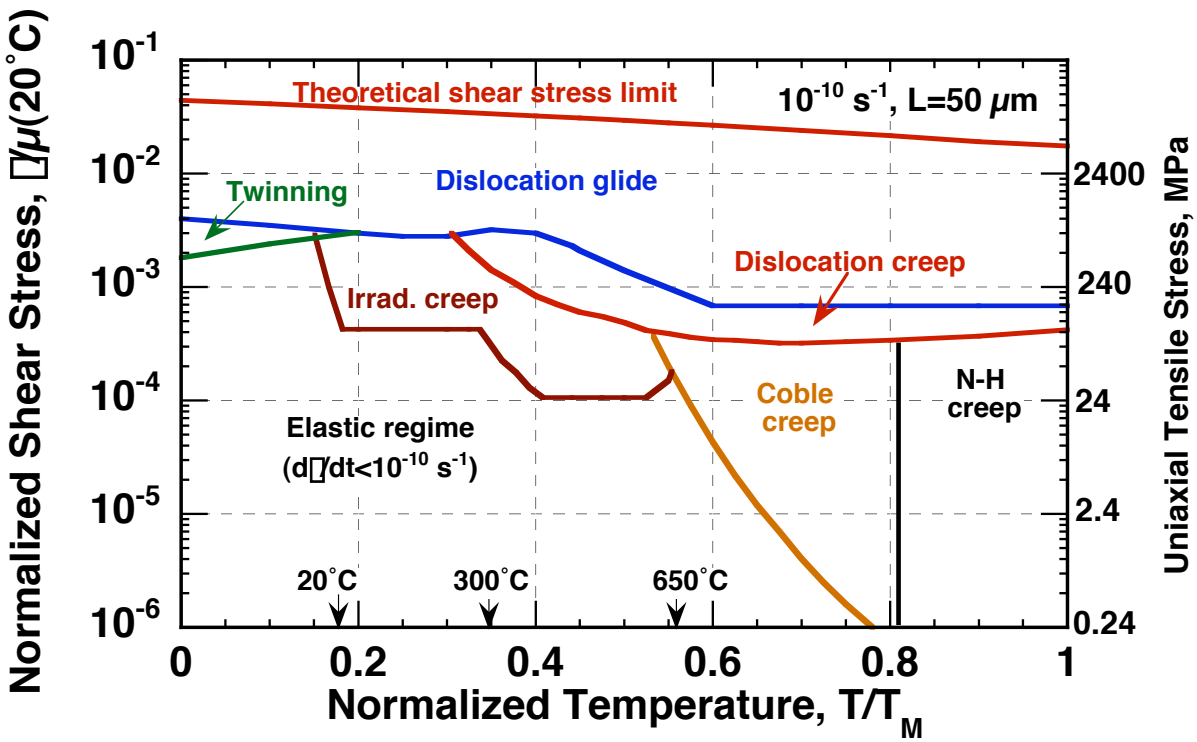

Fig. 13. Deformation map for Type 316 austenitic stainless steel irradiated to 1 dpa for a plastic strain rate of 10^{-10} s^{-1}. The map was constructed assuming τ_0=240 MPa, H_0=1.0 eV, V=120 b^3, τ_f=0 and τ_2=15 MPa.

The main effect of the lower strain rate is that irradiation creep becomes the dominant deformation mode for temperatures up to ~600˚C. At higher temperatures, an expanded Coble creep regime controls the deformation behavior. The appropriate value for the grain boundary frictional stress (τ_f) of irradiated stainless steel at high temperatures is uncertain. Due to accumulation of helium bubbles at grain boundaries, the grain boundary frictional stress should be significantly smaller than for unirradiated stainless steel. A value of τ_f=0 was used for Fig. 13 (same as for Figs. 11, 12).

6. Fracture mechanisms in unirradiated and irradiated metals

As with deformation maps, Ashby-type *fracture* maps are useful for analyzing mechanical behavior in materials. The methodology for determining the boundary lines between the various fracture mechanisms is to compute or empirically determine the conditions which produce equivalent rupture times for the competing processes. Constraint, notch acuity and strain rate effects are all important factors which must be considered in the construction of fracture maps. However, unlike deformation maps, the constitutive equations for fracture are not well established for many of the fracture mechanisms. Therefore, most of the existing fracture maps [140-143] are empirical in nature. A preliminary Ashby fracture mechanism map for neutron irradiated austenitic stainless steel was previously reported by Grossbeck et al. [144]. Some of the relevant constitutive equations for fracture are summarized elsewhere [143,145].

At least seven different fracture mechanisms can be envisioned, several of which may be significantly altered by irradiation. The fracture mechanisms include 1,2) brittle transgranular cleavage or brittle intergranular fracture for $\sigma > \sigma_{crit}(\dot{\varepsilon})$, depending on the relative fracture strength of the grain boundary and matrix. Three subset fracture mechanisms were identified by Gandhi and Ashby [141] for this condition, depending on whether critical-sized pre-existing flaws or cracks were present (Type 1), slip or twin-nucleated cracking occurred (Type 2), or brittle failure was initiated following some general plastic deformation (Type 3). It is well established that radiation hardening promotes cleavage fracture in BCC metals and alloys. It is also possible that radiation induced solute segregation to grain boundaries could

modify the grain boundary fracture strength. It has been suggested that localized flow associated with dislocation channeling in irradiated and deformed materials may create high stresses at grain boundaries which could initiate brittle fracture [38]. 3,4) Ductile intergranular or transgranular fracture (microvoid growth and coalescence) typically occurs at high stresses and low to medium temperatures. Processes such as shear fracture (void sheeting) are a specialized subset of this fracture mechanism. Second phase particles are often the initiation sites for ductile fracture due to localized enhanced stress. Radiation induced solute segregation, radiation induced precipitation, and radiation hardening can affect this fracture process. 5) Transgranular creep fracture typically occurs at elevated temperatures and intermediate stresses. 6) Intergranular creep fracture occurs at elevated temperatures and low stresses. This mechanism generally becomes increasing important with increasing creep lifetimes. Helium grain boundary embrittlement is a very important fracture mechanism in irradiated materials for temperatures above ~0.5 T_M. It is discussed in more detail in the following paragraph. 7) If void nucleation is suppressed during deformation, ductile rupture due to unstable necking is a viable fracture mechanism (although generally not observed). The controversial phenomenon of low temperature He-enhanced embrittlement, which has been reported to occur in ferritic-martensitic steels, needs further validation to determine if it is a new radiation-induced fracture mechanism that is different from normal matrix hardening effects.

Three mechanistic regimes for creep rupture lifetimes due to He embrittlement effects were identified by Trinkaus [134]: Gas-creep driven growth (bubble coalescence) dominates at high He production rates, moderate temperatures, and high stresses, and the kinetics are controlled by the He diffusivity which is equal to the vacancy diffusivity in this regime. Creep constrained growth dominates at low stresses over a broad range of He production rates (high bubble densities on differently oriented grain boundaries causing inhomogeneous creep). Finally, diffusion-controlled growth dominates at low He production rates, high temperatures, and intermediate stresses, and the kinetics are controlled by He bubble dissociation. For conditions appropriate for fusion reactor first wall and blanket structural materials, the time to rupture for He embrittlement is usually controlled by creep constrained cavity growth rather than by gas driven bubble growth.

7. Conclusions

Pronounced matrix hardening is produced by low-temperature (<0.3T_M) irradiation of FCC and BCC metals. This hardening causes an increase in the ductile to brittle transition temperature and a decrease in the fracture toughness of BCC metals, even at temperatures above the DBTT. The fracture toughness of FCC metals is also typically degraded by low-temperature irradiation, although several examples exist where fracture toughness degradation did not occur in radiation hardened FCC alloys (e.g., CuCrZr and 316 stainless steel irradiated at 50-100˚C, at least for doses of 0.3-3 dpa where concomitant substantial loss of tensile uniform elongation occurs). Evidence obtained from several studies suggests that the amount of radiation hardening may be higher in fine-grained materials compared to coarse-grained or single crystal materials. Further work is needed to determine the physical phenomena responsible for this apparent "radiation-modified Hall-Petch" effect.

Radiation-induced tensile "embrittlement" (loss of uniform elongation following low temperature irradiation) is not a reliable indicator of fracture toughness embrittlement. Numerous discrepancies exist in both FCC and BCC alloys where high tensile toughness occurs in materials with low fracture toughness and vice versa.

Ashby deformation maps are a useful framework for categorizing the effects of irradiation on the mechanical deformation of FCC and BCC metals. At low irradiation temperatures, radiation hardening produces an increase in the stress required to induce dislocation glide. Under these irradiation conditions, the plastic instability associated with dislocation channeling can be recognized to be a special case of ordinary dislocation glide, the unique feature being that the irradiation-produced microstructural obstacles to dislocation glide are heterogeneously eliminated during the deformation process. The second major feature of irradiation is to introduce an irradiation creep regime in the deformation maps at low strain rates. Irradiation creep is typically the dominant deformation process at moderate stresses up to ~0.5 T_M in both FCC and BCC metals for typical reactor displacement rates of ~10^{-6} dpa/s. Further work is needed to determine whether cavitation processes associated with high temperature He embrittlement introduce any new deformation mechanisms.

Acknowledgements

This research was sponsored by the Office of Fusion Energy Sciences, U.S. Department of Energy under contract DE-AC05-00OR22725 with UT-Battelle, LLC and by grant number DE-FG03-94ER54275 with the University of California-Santa Barbara.

References

[1] T.J. Koppenaal and R.J. Arsenault, Neutron-irradiation-strengthening in fcc single crystals, Metall. Reviews 16 (1971) 175-196.
[2] M.S. Wechsler, Dislocation channeling in irradiated and quenched metals, in R.E. Reed-Hill (ed.) The Inhomogeneity of Plastic Deformation, Am. Society for Metals, Metals Park, OH, 1972, pp. 19-54.
[3] M.J. Makin, Radiation damage in face centered cubic metals and alloys, in W.F. Sheely (ed.) Radiation Effects (Metallurgical Society Conf. Vol. 37), Gordon and Breach, New York, 1967, pp. 627-669.
[4] J. Diehl and G.P. Seidel, Effect of alloying and cold work on the neutron irradiation hardening of metals, in Radiation Damage in Reactor Materials vol. I, IAEA, Vienna, 1969, pp. 187-214.
[5] A.K. Seeger, On the theory of radiation damage and radiation hardening, in 2nd UN Conf. on Peaceful Uses of Atomic Energy vol. 6, United Nations, New York, 1958, pp. 250-273.
[6] A.L. Bement, Jr., Fundamental materials problems in nuclear reactors, in W.C. Leslie (ed.) 2nd Int. Conf. on Strength of Metals and Alloys vol. II, Am. Society for Metals, Metals Park, OH, 1970, pp. 693-728.
[7] J. Diehl and W. Schilling, Hardening of face-centered cubic metals due to reactor irradiation, in 3rd Intern. Conf. on Peaceful Uses of Atomic Energy vol. 9, United Nations, New York, 1965, pp. 72-77.
[8] T.H. Blewitt, R.R. Coltman, R.E. Jamison and J.K. Redman, (Radiation hardening of copper single crystals), J. Nucl. Mater. 2 (1960) 277-298.
[9] M.A. Adams and P.R.B. Higgins, The hardening of copper by neutron irradiation, Philos. Mag. 4 (1959) 777-780.
[10] G.R. Odette and G.E. Lucas, Analysis of cleavage fracture potential of martensitic stainless steel fusion structures, J. Nucl. Mater. 117 (1983) 264-275.
[11] R.L. Klueh and D.J. Alexander, Embrittlement of Cr-Mo steels after low fluence irradiation in HFIR, J. Nucl. Mater. 218 (1995) 151-160.
[12] G.R. Odette, E. Donahue, G.E. Lucas and J.W. Sheckerd, The effects of constraint, loading rate and irradiation on the toughness-temperature behavior of a V-4Cr-4Ti alloy, in R.K. Nanstad et al. (eds.), 18th Int. Symp. on Effects of Radiation on Materials, ASTM STP 1325, American Society for Testing and Materials, West Conshohocken, PA, 1999, pp. 1089-1108.
[13] S.J. Zinkle et al., Research and development on vanadium alloys for fusion applications, J. Nucl. Mater. 258-263 (1998) 205-214.
[14] F.A. Garner and D.S. Gelles, Irradiation creep mechanisms: an experimental perspective, J. Nucl. Mater. 159 (1988) 286-309.
[15] M.L. Grossbeck, L.T. Gibson, S. Jitsukawa, L.K. Mansur and L.J. Turner, Irradiation creep at temperatures of 400˚C and below for application to near-term fusion devices, in R.K. Nanstad et al. (eds.), 18th Int. Symp. on Effects of Radiation on Materials, ASTM STP 1325, American Society for Testing and Materials, West Conshohocken, PA, 1999, pp. 725-741.
[16] H. Ullmaier, The influence of helium on the bulk properties of fusion reactor structural materials, Nuclear Fusion 24 (1984) 1039-1083.
[17] H. Schroeder and H. Ullmaier, Helium and hydrogen effects on the embrittlement of iron- and nickel-based alloys, J. Nucl. Mater. 179-181 (1991) 118-124.
[18] M.F. Ashby, A first report on deformation-mechanism maps, Acta Metall. 20 (1972) 887-897.
[19] A.S. Kruglov, V.N. Bykov, I. El-Shanshuri and K. Gaber, Effect of neutron irradiation on the yield point of solid copper-based solutions, Sov. Atomic Energy 26 (1969) 582-584.
[20] I.A. El-Shanshoury, The effect of alloying on the neutron-irradiation hardening of copper, J. Nucl. Mater. 45 (1972) 245-257.

[21] H.G. Mohamed, A.M. Hammad and F.H. Hammad, Hardening of copper by solid solution and neutron irradiation, Trans. Indian Inst. Metals 35 (1982) 258-262.
[22] W. Vandermeulen, V. Massaut, J. Van der Velde and W. Hendrix, The effect of irradiation at 150 and 300˚C on the tensile properties of Cu and CuCrZr, in 14th Symp. on Fusion Technology, Pergamon Press, New York, 1986, pp. 1031-1035.
[23] H.L. Heinisch, Effects of the neutron spectrum on mechanical property changes in low dose irradiations, J. Nucl. Mater. 155-157 (1988) 121-129.
[24] S.A. Fabritsiev et al., The Effect of Neutron Spectrum on the Mechanical and Physical Properties of Pure Copper and Copper Alloys, J. Nucl. Mater. 233-237 (1996) 526-533.
[25] B.N. Singh, D.J. Edwards and P. Toft, Effects of neutron irradiation on mechanical properties and microstructures of dispersion and precipitation hardened copper alloys, J. Nucl. Mater. 238 (1996) 244-259.
[26] S.J. Zinkle and L.T. Gibson, Electrical conductivity and tensile properties of copper and oxide dispersion strengthened copper alloys following HFIR irradiation to 13 dpa at 200 and 400˚C, in Fusion Materials Semiann. Prog Rep. for period ending Dec. 31 1999, DOE/ER-0313/27, Oak Ridge National Lab, 1999, pp. 163-174.
[27] J.C. Wilson, Hardening of copper by solid solution and neutron irradiation, in 2nd UN International Conference on Peaceful Uses of Atomic Energy vol. 5: Properties of Reactor Materials, United Nations, New York, 1958, pp. 431-445.
[28] G.E. Lucas, The evolution of mechanical property changes in irradiated austenitic stainless steel, J. Nucl. Mater. 206 (1993) 287-305.
[29] J.P. Robertson, R.L. Klueh, K. Shiba and A.F. Rowcliffe, Radiation hardening and deformation behavior of irradiated ferritic-martensitic Cr-steels, in Fusion Materials Semiann. Prog. Report for period ending Dec. 31 1997, DOE/ER-0313/23, Oak Ridge National Lab, 1997, pp. 179-187.
[30] S.J. Zinkle, L.L. Snead, A.F. Rowcliffe, D.J. Alexander and L.T. Gibson, Effect of irradiation temperature and strain rate on the mechanical properties of V-4Cr-4Ti irradiated to low doses in fission reactors, in Fusion Materials Semiann. Prog. Report for period ending June 30 1998, DOE/ER-0313/24, Oak Ridge National Lab, 1998, pp. 33-40.
[31] U.F. Kocks, The theory of an obstacle-controlled yield strength-report after an international workshop, Mater. Sci. Eng. 27 (1977) 291-298.
[32] S.J. Zinkle, Fundamental radiation effects parameters in metals and ceramics, Radiation Effects and Defects in Solids 148 (1999) 447-477.
[33] S. Kojima, S.J. Zinkle and H.L. Heinisch, Radiation hardening in neutron-irradiated polycrystalline copper: barrier strength of defect clusters, J. Nucl. Mater. 179-181 (1991) 982-985.
[34] Y. Dai and M. Victoria, Defect cluster structure and tensile properties of copper single crystals irradiated with 600 MeV protons, in I.M. Robertson et al. (eds.), Microstructure Evolution During Irradiation, MRS Symposium Proceedings vol. 439, Materials Research Society, Pittsburgh, 1997, pp. 319-324.
[35] S.J. Zinkle and R.L. Sindelar, Defect microstructures in neutron-irradiated copper and stainless steel, J. Nucl. Mater. 155-157 (1988) 1196-1200.
[36] P.M. Rice and S.J. Zinkle, Temperature dependence of radiation damage microstructure in V-4Cr-4Ti neutron irradiated to low dose, J. Nucl. Mater. 258-263 (1998) 1414-1419.
[37] B.N. Singh and S.J. Zinkle, Defect accumulation in pure fcc metals in the transient regime: a review, J. Nucl. Mater. 206 (1993) 212-229.
[38] M. Victoria et al., The microstructure and associated tensile properties of irradiated fcc and bcc metals, J. Nucl. Mater. 276 (2000) 114-122.
[39] A.J.E. Foreman and M.J. Makin, Dislocation movement through random arrays of obstacles, Philos. Mag. 14 (1966) 911-924.
[40] G.R. Odette, G.E. Lucas, G. Tedeski and B.D. Wirth, Development of superposition rules for hardening in alloys containing multiple defect populations, in Fusion Materials Semiann. Prog Rep. for period ending Dec. 31 1998, DOE/ER-0313/25, Oak Ridge National Lab, 1998, pp. 221-226.
[41] U.F. Kocks, The relation between polycrystal deformation and single-crystal deformation, Metall. Trans. 1 (1970) 1121-1143.
[42] M.J. Makin and S.A. Manthorpe, Hardening of copper irradiated at -195˚C, Acta Metall. 9 (1961) 886-888.

[43] S. Kojima, S.J. Zinkle and H.L. Heinisch, Grain size effect on radiation hardening in neutron-irradiated polycrystalline copper, in Fusion Reactor Materials Semiannual Progress Report for Period ending March 31, 1989, DOE/ER-0313/6, 1989, pp. 43-49.
[44] M.S. Wechsler, in The Interaction of Radiation with Solids, North-Holland, Amsterdam, 1964, pp. 246-.
[45] G.P. Seidel, Phys. Stat. Sol. 25 (1968) 175.
[46] M.J. Makin and J.V. Sharp, A model of "lattice" hardening in irradiated copper crystals with the external characteristics of "source" hardening, Phys. Stat. Sol. 9 (1965) 109-118.
[47] B.N. Singh, A.J.E. Foreman and H. Trinkaus, Radiation hardening revisited: role of intracascade clustering, J. Nucl. Mater. 249 (1997) 103-115.
[48] N. Baluc, C. Bailat, Y. Dai, M.I. Luppo, R. Schaublin and M. Victoria, A comparison of the microstructure and tensile behaviour of irradiated fcc and bcc metals, in S.J. Zinkle et al. (eds.), Microstructural Processes During Irradiation, MRS Symposium Proceedings vol. 540, Materials Research Society, Warrendale, PA, 1999, pp. 539-548.
[49] J.L. Brimhall and B. Mastel, Deformation structure in neutron-irradiated copper-aluminum alloy, Appl. Phys. Lett. 9 (1966) 127-128.
[50] J.V. Sharp, Deformation of neutron-irradiated copper single crystals, Philos. Mag. 16 (1967) 77-96.
[51] J.V. Sharp, Correlation between cleared channels and surface slip steps in neutron irradiated copper crystals, Radiat. Eff. 14 (1972) 71-75.
[52] L.M. Howe, Irradiation hardening and annealing in copper at high neutron fluences, Radiat. Eff. 23 (1974) 181-195.
[53] A. Okada, K. Kanao, T. Yoshiie and S. Kojima, Transition of deformation structures in Ni and Au by D-T neutron irradiation, Mater. Trans. JIM 30 (1989) 265-272.
[54] A. Luft, Microstructural processes of plastic instabilities in strengthened metals, Progress in Materials Science 35 (1991) 97-204.
[55] R.J. Arsenault and J. Bressers, A comparison of the effect of neutron irradiation on high purity vanadium and vanadium oxygen alloys, Metall. Trans. 8A (1977) 925-931.
[56] I.G. Greenfield and H.G.F. Wilsdorf, Effect of neutron irradiation on the plastic deformation of copper single crystals, J. Appl. Phys. 32 (1961) 827-839.
[57] U. Essmann and A. Seeger, Verfestigungsverhalten neutronenbestrahlter Metall - II: Temperaturwechselversuche und Gleitlinienbeobachtungen an Kupfereinkristallen, Phys. Stat. Sol. 4 (1964) 177-197.
[58] J.L. Brimhall, The effect of neutron irradiation on slip lines in molybdenum, Trans. Metall. Soc. AIME 233 (1965) 1737.
[59] B. Mastel, H.E. Kissinger, J.J. Laidler and T.K. Bierlein, Dislocation channeling in neutron-irradiated molybdenum, J. Appl. Phys. 34 (1963) 3637.
[60] R.P. Tucker, S.M. Ohr and M.S. Wechsler, Radiation hardening and transmission electron microscopy in niobium, in Radiation Damage in Reactor Materials vol. I, IAEA, Vienna, 1969, pp. 215-233.
[61] R.P. Tucker, M.S. Wechsler and S.M. Ohr, Dislocation channeling in neutron-irradiated niobium, J. Appl. Phys. 40 (1969) 400.
[62] F.A. Smidt, Jr., Dislocation channeling in irradiated metals, Naval Research Lab, Washington DC Report NRL-7078, 1970.
[63] K. Noda, H. Saka, K. Shiraishi, H. Yoshida and T. Imura, In-situ studies of dynamic formation of dislocation channels in neutron-irradiated Ni by HVEM, in Proc. 5th Intern. Conf. on High Voltage Electron Microscopy, Kyoto, Japanese Soc. of Electron Microscopy, Tokyo, 1977, pp. 403-406.
[64] E. Johnson and P.B. Hirsch, In situ straining in the HVEM of neutron-irradiated copper crystals, Philos. Mag. A 43 (1981) 157-170.
[65] E.H. Lee, T.S. Byun, J.D. Hunn, M.H. Yoo, K. Farrell and L.K. Mansur, On the origin of deformation microstructures in austenitic stainless steel: Part I–Microstructures, Acta Mater. 49 (2001) 3269-3276.
[66] N. Hashimoto, S.J. Zinkle, A.F. Rowcliffe, J.P. Robertson and S. Jitsukawa, Deformation mechanisms in 316 stainless steel irradiated at 60˚C and 330˚C, J. Nucl. Mater. 283-287 (2000) 528-534.

[67] J.L. Brimhall, J.I. Cole, J.S. Vetrano and S.M. Bruemmer, Temperature and strain-rate effects on deformation mechanisms in irradiated stainless steel, in I.M. Robertson et al. (eds.), Microstructure of Irradiated Materials, MRS Symposium Proceedings vol. 373, Materials Research Society, Pittsburgh, 1995, pp. 177-182.
[68] S.M. Bruemmer, J.I. Cole, R.D. Carter and G.S. Was, Defect microstructures and deformation mechanisms in irradiated austenitic stainless steels, in I.M. Robertson et al. (eds.), Microstructure Evolution During Irradiation, MRS Symposium Proceedings vol. 439, Materials Research Society, Pittsburgh, 1997, pp. 437-444.
[69] K. Farrell, T.S. Byun and N. Hashimoto, Mapping flow localization processes in deformation of irradiated reactor structural alloys, Oak Ridge National Lab, Oak Ridge, TN Report ORNL/TM-2002/66, 2002.
[70] S.J. Zinkle, T.S. Byun, K. Farrell and N. Hashimoto, Review of Experimental Studies of Deformation Mechanisms in Irradiated Metals, 2nd IEA Fusion Materials Workshop on Modeling and Experimental Validation, Les Diablerets, Switzerland, Sept. 30-Oct. 4, 2002; to be submitted to J. Nucl. Mater. (2003).
[71] M.L. Grossbeck, K. Ehrlich and C. Wassilew, An assessment of the tensile, irradiation creep, creep rupture, and fatigue behavior in austenitic stainless steels with emphasis on spectral effects, J. Nucl. Mater. 174 (1990) 264-281.
[72] F.A. Garner, M.B. Toloczko and B.H. Sencer, Comparison of swelling and irradiation creep behavior of fcc-austenitic and bcc-ferritic/martensitic alloys at high neutron exposure, Journal of Nuclear Materials 276 (2000) 123-142.
[73] H. Trinkaus and H. Ullmaier, High temperature embrittlement of metals due to helium: is the lifetime dominated by cavity growth or crack growth?, J. Nucl. Mater. 212-215 (1994) 303-309.
[74] G.J.C. Carpenter and R.B. Nicholson, High-temperature embrittlement of metals by rare gas bubbles, in Radiation Damage in Reactor Materials vol. II, IAEA, Vienna, 1969, pp. 383-400.
[75] S.J. Zinkle, A brief review of radiation-induced cavity swelling and hardening in copper and copper alloys, in R.E. Stoller, A.S. Kumar and D.S. Gelles (eds.), 15th Int. Symp. on Effects of Radiation on Materials, ASTM STP 1125, American Society for Testing and Materials, Philadelphia, 1992, pp. 813-834.
[76] S.J. Zinkle and N.M. Ghoniem, Operating temperature windows for fusion reactor structural materials, Fusion Eng. Design 49-50 (2000) 709-717.
[77] J.P. Robertson, I. Ioka, A.F. Rowcliffe, M.L. Grossbeck and S. Jitsukawa, Temperature dependence of the deformation behavior of type 316 stainless steel after low temperature neutron irradiation, in R.K. Nanstad et al. (eds.), 18th Int. Symp. on Effects of Radiation on Materials, ASTM STP 1325, American Society for Testing and Materials, West Conshohocken, PA, 1999, pp. 671-688.
[78] S.J. Zinkle and S.A. Fabritsiev, Copper Alloys for High Heat Flux Structure Applications, Atomic and Plasma-Material Interaction Data for Fusion (supplement to Nuclear Fusion) 5 (1994) 163-192.
[79] D.J. Edwards, S.J. Zinkle, S.A. Fabritsiev and A.S. Pokrovsky, Round robin comparison of tensile results on GlidCop Al25, in Fusion Materials Semiannual Progress Report for Period ending June 30, 1998, DOE/ER-0313/24, Oak Ridge National Lab, 1998, pp. 193-199.
[80] E.V. van Osch, M.G. Horsten and M.I. de Vries, Irradiation testing of 316L(N)-IG austenitic stainless steel for ITER, J. Nucl. Mater. 258-263 (1998) 301-307.
[81] J.E. Pawel, A.F. Rowcliffe, G.E. Lucas and S.J. Zinkle, Irradiation performance of stainless steels for ITER application, J. Nucl. Mater. 239 (1996) 126-131.
[82] M.G. Horsten and M.I. de Vries, Irradiation hardening and loss of ductility of type 316L(N) stainless steel plate material due to neutron irradiation, in D.S. Gelles et al. (eds.), 17th Int. Symp. on Effects of Radiation on Materials, ASTM STP 1270, American Society for Testing and Materials, West Conshohocken, PA, 1996, pp. 919-932.
[83] S.J. Zinkle, P.J. Maziasz and R.E. Stoller, Dose dependence of the microstructural evolution in neutron-irradiated austenitic stainless steel, J. Nucl. Mater. 206 (1993) 266-286.
[84] R.L. Fish, J.L. Straalsund, C.W. Hunter and J.J. Holmes, Swelling and tensile property evaluation of high-fluence EBR-II thimbles, in J. Moteff (ed.) Effects of radiation on substructure and mechanical properties of metals and alloys, ASTM STP 529, American Society for Testing and Materials, Philadelphia, 1973, pp. 149-164.
[85] S. Tähtinen, M. Pyykkönen, P. Karjalainen-Roikonen, B.N. Singh and P. Toft, Effect of neutron irradiation on fracture toughness behavior of copper alloys, J. Nucl. Mater. 258-263 (1998) 1010-1014.

[86] S. Tähtinen, M. Pyykkönen, B.N. Singh and P. Toft, Effect of neutron irradiation on tensile and fracture toughness properties of copper alloys and their joints with stainless steel, in M.L. Hamilton et al. (eds.), 19th Int. Symp. on Effects of Radiation on Materials, ASTM STP 1366, American Society for Testing and Materials, West Conshohocken, 2000, pp. 1243-1259.
[87] D.J. Alexander, J.E. Pawel, M.L. Grossbeck, A.F. Rowcliffe and K. Shiba, Fracture toughness of irradiated candidate materials for ITER first wall/blanket structures, in D.S. Gelles et al. (eds.), 17th Int. Symp. on Effects of Radiation on Materials, ASTM STP 1270, American Society for Testing and Materials, West Conshohocken, PA, 1996, pp. 945-970.
[88] A.F. Rowcliffe et al., Fracture toughness and tensile behavior of ferritic-martensitic steels irradiated at low temperatures, J. Nucl. Mater. 258-263 (1998) 1275-1279.
[89] L.L. Snead, S.J. Zinkle, D.J. Alexander, A.F. Rowcliffe, J.P. Robertson and W.S. Eatherly, Temperature dependence of the tensile and impact properties of V-4Cr-4Ti irradiated to low neutron doses, in Fusion Materials Semiann. Prog. Report for period ending Dec. 31 1997, DOE/ER-0313/23, Oak Ridge National Lab, 1997, pp. 81-98.
[90] F.R.N. Nabarro and H.L. de Villiers, The Physics of Creep, Taylor and Francis, London, 1995.
[91] S.M. Ohr, R.P. Tucker and M.S. Wechsler, Radiation hardening in bcc metals niobium and iron, Trans. JIM 9 Supplement (Proc. ICSMA-1) (1968) 187-192.
[92] S. Yoshida, M. Kiritani, Y. Deguchi and N. Kamigaki, Hardening and recovery of quenched gold, Trans.JIM9 Supplement(Proc.ICSMA-1)(1968)83 [93]J.W. Christian and S. Mahajan, Deformation twinning, Progress in Materials Science 39 (1995) 1-158.
[94] O.D. Sherby and A.K. Miller, Combining phenomenology and physics in describing the high temperature mechanical behavior of crystalline solids, J. Eng. Mater. and Technol. 101 (1979) 387-395.
[95] K.C. Russell and F.H. Froes, Dispersoid formation and stability in alloys, Journal of Metals (March, 1988) 29-35.
[96] B. Burton, The influence of alumina dispersions on the diffusion creep behaviour of polycrystalline copper, Met. Sci. J. 5 (1971) 11-14.
[97] J. Rösler and E. Artz, A new model-based creep equation for dispersion strengthened materials, Acta Metall. Mater. 38 (1990) 671-683.
[98] M.W. Guinan and D.J. Steinberg, Pressure and temperature derivatives of the isotropic polycrystalline shear modulus for 65 elements, J. Phys. Chem. Solids 35 (1974) 1501-1512.
[99] D.B. Butrymowicz, J.R. Manning and M.E. Read, Diffusion in Copper and Copper Alloys, J. Phys. Chem. Ref. Data 2 (1973) 643-656.
[100] H.E. Schaefer, Positron annihilation spectroscopy of defects in metals, in P.G. Coleman, S.C. Sharma and L.M. Diana (eds.), Positron Annihilation, North-Holland, New York, 1982, pp. 369-380.
[101] J.P. Hammond, et al., Dynamic and Static Measurements of Elastic Constants with Data on 2-1/4Cr-1Mo Steel, Types 304 and 316 Stainless Steels, and Alloy 800H, Oak Ridge National Laboratory, Oak Ridge, TN Report ORNL-5442, 1979.
[102] W.A. Simpson, Room temperature elastic properties of V-5Cr-5Ti, in Fusion Materials Semiannual Progress Report for Period ending March 31, 1994, DOE/ER-0313/16, Oak Ridge National Lab, 1994, pp. 258-259.
[103] R.J. Farraro and R.B. McLellan, High temperature elastic properties of polycrystalline niobium, tantalum and vanadium, Metall. Trans. 10A (1979) 1699-1702.
[104] H. Schultz, Defect parameters of bcc metals: group-specific trends, Mater. Sci. Eng. A141 (1991) 149-167.
[105] K. Shiba, A. Hishinuma, A. Tohyama and K. Masamura, Properties of Low Activation Ferritic Steel F82H IEA Heat - Interim Report of IEA Round-Robin Tests (1), Japan Atomic Energy Research Institute Report JAERI-Tech 97-038, 1997.
[106] P.C.J. Gallagher, The influence of alloying, temperature, and related effects on the stacking fault energy, Metall. Trans. 1 (1970) 2429-2461.
[107] R.M. Latanision and A.W. Ruff, Jr., The temperature dependence of stacking fault energy in Fe-Cr-Ni alloys, Metall. Trans. 2 (1971) 505-509.
[108] M.S. Duesbury and V. Vitek, Plastic anisotropy in BCC transition metals, Acta Mater. 46 (1998) 1481-1492.
[109] R.S. Mishra, H. Jones and G.W. Greenwood, On the threshold stress for diffusional creep in pure metals, Philos. Mag. A 60 (1989) 581-590.

[110] G. Martin and B. Perrailllon, Measurements of grain boundary diffusion, in R.W. Balluffi (ed.) Grain-boundary structure and kinetics, American Society for Metals, Materials Park, OH, 1980, pp. 239-295.
[111] R.E. Gold, D.L. Harrod, R.L. Ammon, R.W. Buckman, Jr. and R.C. Svedberg, Technical assessment of vanadium-base alloys for fusion reactor applications, Vols. 1 & 2, Westinghouse Electric Corporation, Pittsburgh Report COO-4540-1, 1978.
[112] H.M. Chung, B.A. Loomis and D.L. Smith, Creep properties of vanadium-base alloys, J. Nucl. Mater. 212-215 (1994) 772-777.
[113] K. Natesan, W.K. Soppett and D.L. Rink, Uniaxial creep behavior of V-4Cr-4Ti alloy, in Fusion Materials Semiann. Prog. Report for period ending June 30 2000, DOE/ER-0313/28, Oak Ridge National Lab, 2000, pp. 39-47.
[114] K. Natesan, W.K. Soppett and D.L. Rink, Uniaxial creep behavior of V-4Cr-4Ti alloy, J. Nucl. Mater. Proc. ICFRM10 (2002) in press.
[115] R.J. Kurtz and M.L. Hamilton, Biaxial thermal creep of V-4Cr-4Ti at 700˚C and 800˚C, in Fusion Materials Semiann. Prog. Report for period ending June 30 1999, DOE/ER-0313/26, Oak Ridge National Lab, 1999, pp. 3-10.
[116] M.L. Grossbeck, R.J. Kurtz, L.T. Gibson and M.J. Gardner, Investigation of the effect of a low-oxygen lithium environment on the creep of the V-4Cr-4Ti alloy, in Fusion Materials Semiann. Prog. Report for period ending June 30 2002, DOE/ER-0313/32, Oak Ridge National Lab, 2002, pp. 6-11.
[117] S. Ukai, T. Nishida, T. Okuda and T. Yoshitake, R&D of oxide dispersion strengthened ferritic/martensitic steels for LMFBR, J. Nucl. Mater. 258-263 (1998) 1745-1749.
[118] R.L. Klueh et al., Tensile and creep properties of an oxide dispersion-strengthened ferritic steel, J. Nucl. Mater. 307-311 (2002) 773-777.
[119] S.J. Zinkle and W.S. Eatherly, Effects of test temperature and strain rate on the tensile properties of high-strength, high-conductivity copper alloys, in Fusion Materials Semiannual Progress Report for Period ending Dec. 31, 1996, DOE/ER-0313/21, Oak Ridge National Lab, 1996, pp. 165-174.
[120] D.J. Edwards, Temperature and strain rate effects in high strength, high conductivity copper alloys tested in air, in Fusion Materials Semiannual Progress Report for Period ending Dec. 31, 1997, DOE/ER-0313/23, Oak Ridge National Lab, 1997, pp. 213-222.
[121] S.J. Zinkle, Tensile properties of high-strength, high-conductivity copper alloys at high temperatures, in Fusion Materials Semiannual Progress Report for Period ending June 30, 2000, DOE/ER-0313/28, Oak Ridge National Lab, 2000, pp. 171-175.
[122] J. Groza, Heat-resistant dispersion-strengthened copper alloys, J. Mater. Eng. and Performance 1 (1992) 113-121.
[123] S.J. Zinkle and W.S. Eatherly, Tensile and Electrical Properties of Unirradiated and Irradiated Hycon 3HP CuNiBe, in Fusion Materials Semiannual Progress Report for Period ending June 30, 1996, DOE/ER-0313/20, Oak Ridge National Lab, 1996, pp. 207-216.
[124] S.J. Zinkle, L.L. Snead, J.P. Robertson and A.F. Rowcliffe, Strain rate dependence of the tensile properties of V-(4-5%)Cr-(4-5%)Ti irradiated in EBR-II and HFBR, in Fusion Materials Semiann. Prog Rep. for period ending Dec. 31 1997, DOE/ER-0313/23, Oak Ridge National Lab, 1997, pp. 77-80.
[125] N. Hashimoto, S.J. Zinkle, R.L. Klueh, A.F. Rowcliffe and K. Shiba, Deformation mechanisms in ferritic/martensitic steels irradiated in HFIR, in G.E. Lucas et al. (eds.), Microstructural Processes During Irradiation-2000, MRS Symposium Proceedings vol. 650, Materials Research Society, Warrendale, PA, 2001, pp. R1.10.11-R11.10.16.
[126] A.F. Rowcliffe, S.J. Zinkle and D.T. Hoelzer, Effect of strain rate on the tensile properties of unirradiated and irradiated V-4Cr-4Ti, J. Nucl. Mater. 283-287 (2000) 508-512.
[127] P. Fenici, D.J. Boerman, G.P. Tartaglia and J.D. Elen, Effect of fast-neutron irradiation on tensile properties of precipitation-hardened Cu-Cr-Zr alloy, J. Nucl. Mater. 212-215 (1994) 399-403.
[128] A.F. Rowcliffe, S.J. Zinkle, J.F. Stubbins, D.J. Edwards and D.J. Alexander, Austenitic Stainless Steels and High Strength Copper Alloys for Fusion Components, J. Nucl. Mater. 258-263 (1998) 183-192.
[129] S.J. Zinkle, J.P. Robertson and R.L. Klueh, Thermophysical and mechanical properties of Fe-(8-9%)Cr reduced activation steels, in Fusion Materials Semiann. Prog. Report for period ending June 30 1998, DOE/ER-0313/24, Oak Ridge National Lab, 1998, pp. 135-143.

[130] K. Ehrlich, Deformation behavior of austenitic stainless steels after and during neutron irradiation, J. Nucl. Mater. 133&134 (1985) 119-126.
[131] R.E. Stoller, M.L. Grossbeck and L.K. Mansur, A theoretical model of accelerated irradiation creep at low temperatures by transient interstitial absorption, in R.E. Stoller, A.S. Kumar and D.S. Gelles (eds.), 15th Int. Symp. on Effects of Radiation on Materials, ASTM STP 1125, American Society for Testing and Materials, Philadelphia, 1992, pp. 517-529.
[132] F.A. Garner, M.B. Toloczko and M.L. Grossbeck, The dependence of irradiation creep in austenitic alloys on displacement rate and helium to dpa ratio, J. Nucl. Mater. 258-263 (1998) 1718-1724.
[133] F.A. Garner and W.G. Wolfer, Factors which determine the swelling behavior of austenitic stainless steels, J. Nucl. Mater. 122&123 (1984) 201-206.
[134] H. Trinkaus, Modeling of helium effects in metals: High temperature embrittlement, J. Nucl. Mater. 133&134 (1985) 105-112.
[135] D.N. Braski, H. Schroeder and H. Ullmaier, The effect of tensile stress on the growth of helium bubbles in an austenitic stainless steel, J. Nucl. Mater. 83 (1979) 265-277.
[136] D.R. Harries, Neutron irradiation-induced embrittlement in type 316 and other austenitic steels and alloys, J. Nucl. Mater. 82 (1979) 2-21.
[137] N. Yamamoto, Y. Murase, J. Nagakawa and K. Shiba, Creep behavior of reduced activation martensitic steel F82H injected with a large amount of helium, J. Nucl. Mater. 307-311 (2002) 217-221.
[138] H. Schroeder, W. Kesternich and H. Ullmaier, Helium effects on the creep and fatigue resistance of austenitic stainless steels at high temperatures, Nucl. Eng. Des./Fusion 2 (1985) 65-95.
[139] R.D. Carter, M. Atzmon, G.S. Was and S.M. Bruemmer, Deformation mechanisms in a proton-irradiated austenitic stainless steel, in I.M. Robertson et al. (eds.), Microstructure of Irradiated Materials, MRS Symposium Proceedings vol. 373, Materials Research Society, Pittsburgh, 1995, pp. 171-176.
[140] M.F. Ashby, C. Gandhi and D.M.R. Taplin, Fracture-mechanism maps and their construction for FCC metals and alloys, Acta Metallurgica 27 (1979) 699-729.
[141] C. Gandhi and M.F. Ashby, Fracture-mechanism maps for materials which cleave: FCC, BCC and HCP metals and ceramics, Acta Metall. 27 (1979) 1565-1602.
[142] R.J. Fields, T. Weerasooriya and M.F. Ashby, Fracture-mechanisms in pure iron, two austenitic steels, and one ferritic steel, Metall. Trans. A 11 (1980) 333-347.
[143] G.D. Quinn, Fracture-mechanism maps for advanced structural ceramics. Part 1. Methodology and hot-pressed silicon nitride results, J. Mater. Sci. 25 (1990) 4361-4376.
[144] M.L. Grossbeck, J.O. Stiegler and J.J. Holmes, Effects of irradiation on the fracture behavior of austenitic stainless steels, in M.L. Bleiberg and J.W. Bennett (eds.), Radiation effects in breeder reactor structural materials, TMS-AIME, New York, 1977, pp. 95-116.
[145] D. Teirlinck, F. Zok, J.D. Embury and M.F. Ashby, Fracture-mechanism maps in stress space, Acta Metall. 36 (1988) 1213-1228.